Cell Reports
Physical Science

Article

Contact lens bioelectronic platform for non-invasive depression treatment with machine-learning-based evaluation

Graphical abstract

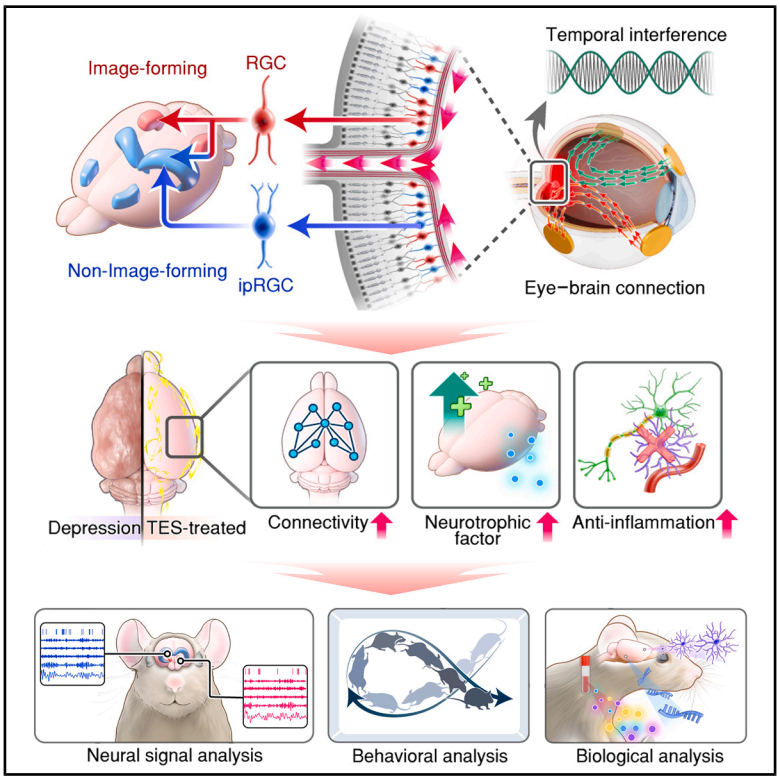

Highlights

- Non-invasive TI-TES modulates brain via the eye-brain pathway
- Contact lens platform restores depression-related dysfunctions
- Transparent ultrathin electrodes ensure wearable ocular integration
- Multimodal machine learning validates therapeutic efficacy

Authors

Wonjung Park, Joonho Paek, Hunkyu Seo, ..., Sumin Kim, Suk Ho Byeon, Jang-Ung Park

Correspondence

jang-ung@yonsei.ac.kr

In brief

Park et al. present a wearable contact lens platform enabling non-invasive neuromodulation via temporal-interference-based transcorneal electrical stimulation. This approach restores behavioral, neural, and biological deficits in depression and integrates machine learning for comprehensive efficacy evaluation.

Park et al., 2026, Cell Reports Physical Science 7, 103303
May 20, 2026
https://doi.org/10.1016/j.xcrp.2026.103303

CellPress

Cell Reports
Physical Science

CellPress
OPEN ACCESS

Article

Contact lens bioelectronic platform for non-invasive depression treatment with machine-learning-based evaluation

Wonjung Park,[1,2,8] Joonho Paek,[1,2,8] Hunkyu Seo,[1,2,8] Yeon-Mi Hong,[1,2,8] Enji Kim,[1,2] Won Gi Chung,[1,2] Seung Hyun An,[1,2] Min Seok Choi,[3,4] Eunmin Kim,[1,2] Jakyoung Lee,[1,2] Inhea Jeong,[1,2] Sumin Kim,[1,2] Suk Ho Byeon,[3,4] and Jang-Ung Park[1,2,5,6,7,9,*]

[1]Department of Materials Science and Engineering, Yonsei University, Seoul 03722, Republic of Korea
[2]Center for Nanomedicine, Institute for Basic Science (IBS), Yonsei University, Seoul 03722, Republic of Korea
[3]Institute of Vision Research, Department of Ophthalmology, Severance Eye Hospital, Yonsei University College of Medicine, Seoul 03722, Republic of Korea
[4]Brain Korea 21 Project for Medical Sciences, Yonsei University College of Medicine, Seoul 03722, Republic of Korea
[5]Department of Neurosurgery, Yonsei University College of Medicine, Seoul 03722, Republic of Korea
[6]Graduate Program of Nano Biomedical Engineering (NanoBME), Advanced Science Institute, Yonsei University, Seoul 03722, Republic of Korea
[7]Yonsei-KIST Convergence Research Institute, Seoul 03722, Republic of Korea
[8]These authors contributed equally
[9]Lead contact
*Correspondence: jang-ung@yonsei.ac.kr
https://doi.org/10.1016/j.xcrp.2026.103303

SUMMARY

Here, we present a wearable, non-invasive contact lens bioelectronic platform designed to enable a more fundamental treatment of depression. Through the implementation of temporal-interference-based transcorneal electrical stimulation (TI-TES), the contact lens platform enables effective delivery of stimulation from the corneal surface to the retina and ultimately to the brain. The TI-TES platform features ultrathin gallium oxide and platinum layers as transparent, flexible electrodes, enabling seamless integration into soft contact lenses. This approach preserves vision and ensures conformal ocular coupling. In a preclinical stress-induced mouse model that recapitulates key behavioral and biological features associated with depression, TI-TES enhanced behavioral resilience, restored prefrontal-hippocampal oscillatory synchrony, and normalized depression-related biomarkers. Machine-learning integration of behavioral, electrophysiological, and biological data consistently distinguished treated from control groups. These preclinical findings establish TI-TES as a non-invasive bioelectronic strategy that overcomes current limitations, enabling selective eye-brain pathway modulation for depression and potentially other brain disorders.

INTRODUCTION

Wearable electronics have advanced rapidly, providing versatile platforms for health monitoring[1–4] and physiological intervention.[5–7] In particular, the development of wearable systems for bioelectrical signal interfacing has been especially pronounced,[8–10] with devices designed to record bioelectrical signals for monitoring various conditions.[11–14] For example, contact lens-based biosignal acquisition has been explored, such as measuring tear glucose or intraocular pressure. These smart contact lens devices enable the non-invasive real-time monitoring of biomarkers, introducing a new paradigm for personalized healthcare. However, most of the smart contact lenses developed to date have been limited to applications in the diagnosis of metabolic diseases or the monitoring and treatment of ocular disorders, leaving broader therapeutic opportunities unexplored. One area that has remained largely unaddressed is the application of contact lens platforms to mental health disorders, such as depression.

Depression is increasingly recognized as a disorder of distributed brain networks, involving structural and functional abnormalities such as reduced limbic volume, disrupted hippocampus (HPC)-prefrontal cortex (PFC) connectivity, and impaired neural plasticity.[15–19] Conventional treatments, including pharmacological therapy, electroconvulsive therapy, and deep brain stimulation, target these abnormalities but are often limited by variable efficacy, invasiveness, or tolerability.[20–23]

The eye provides a compelling gateway for indirect brain modulation due to its embryological derivation from the brain[24] and its extensive connectivity with both image-forming pathways, including the primary visual cortex, and non-image-forming circuits implicated in mood regulation, such as the HPC, PFC, and amygdala.[25,26] Epidemiological evidence linking visual impairment with higher prevalence of depression further

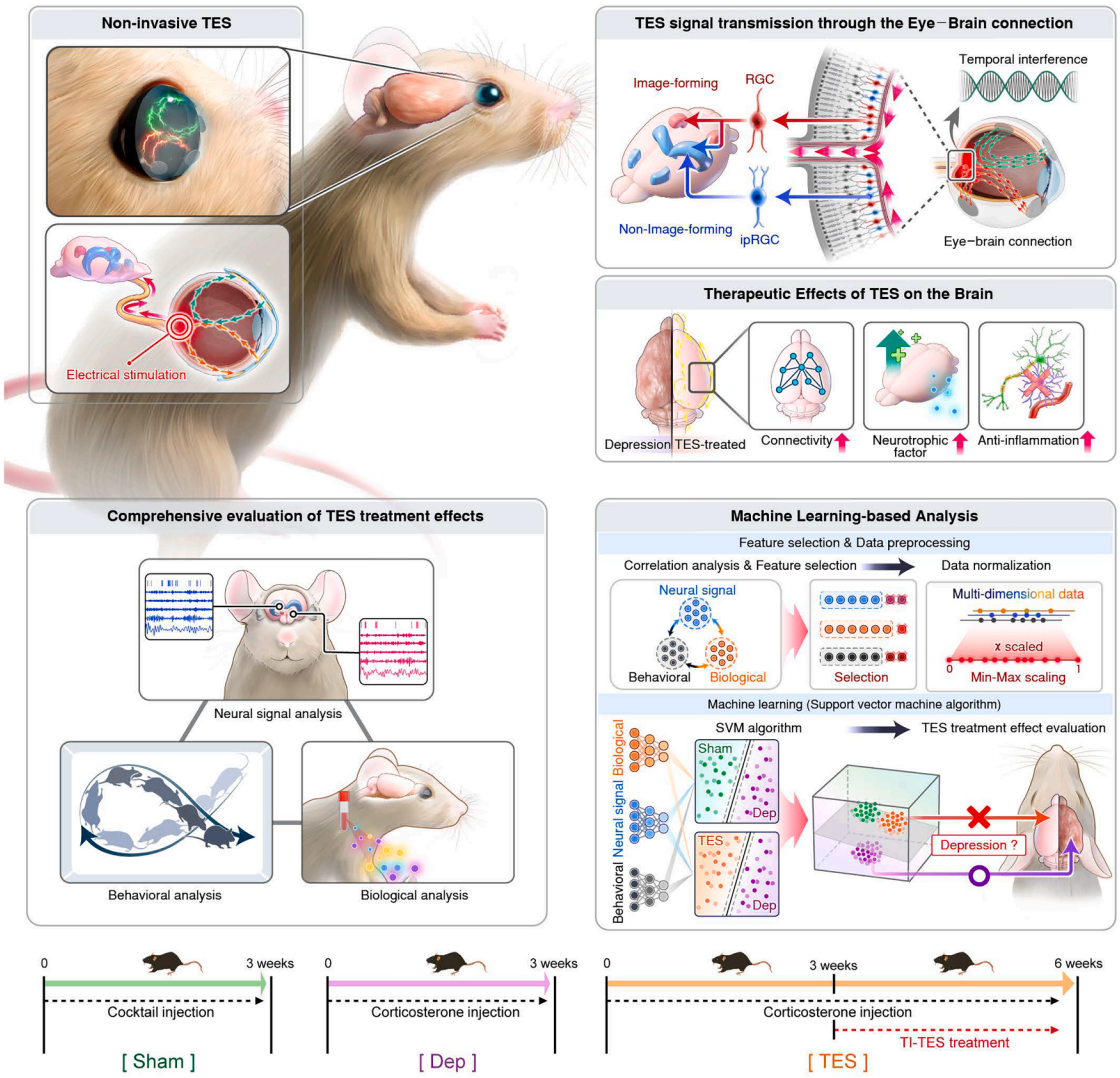

Figure 1. Conceptual framework and evaluation strategy of a contact lens-based TI-TES system for depression treatment

Schematic overview of a contact lens-based TI-TES system for depression treatment, illustrating the stimulation principle, eye-brain neural pathway, and therapeutic evaluation using machine learning.

emphasizes the functional relevance of the eye-brain axis.[27,28] Nevertheless, existing ocular electrical stimulation approaches are largely limited to ocular disease treatment[29] and rely on bulky corneal-periocular electrodes that are impractical for chronic or repeated use.[30]

Here, we present a soft, wearable contact lens with a temporal-interference-based transcorneal electrical stimulation (TI-TES) system designed for non-invasive depression therapy. All electrodes are integrated into a single transparent lens, enabling conformal contact with the cornea while preserving natural vision. To ensure both transparency and high flexibility for wearability, the electrodes were constructed on an ultrathin gallium oxide layer with platinum (Pt) decoration. This lens delivers temporal interference (TI) stimulation, in which two high-frequency electrical signals intersect at the retina to generate a low-frequency envelope field, enabling targeted modulation of deeper eye-brain circuits while minimizing off-target stimulation.[31–34] To reduce impedance and improve charge transfer as well as stimulation efficiency, Pt nanocluster coatings are applied to the electrodes.[35,36]

To comprehensively evaluate the therapeutic effects of our TI-TES contact lens, we employed a multidomain assessment framework that included electrophysiological brain recordings. To minimize tissue damage and preserve recording integrity, we fabricated an exceptionally soft neural probe using liquid metal and a fluorinated elastomer, materials chosen for their mechanical compliance with brain tissue. We evaluated this TI-TES platform in a corticosterone-induced mouse model recapitulating depression-associated phenotypes using multiple assessment approaches. Behavioral assays measured both individual and social-depression-related phenotypes. Electrophysiological brain recordings quantified HPC-PFC functional connectivity.

Molecular analyses examined mRNA expression, neuronal histology, and stress-related hormone levels. A machine-learning pipeline was then applied to integrate these behavioral, electrophysiological, and biological datasets, enabling high-dimensional pattern recognition and multiparametric classification of individual animals. TI-TES-treated mice consistently clustered apart from depression controls, revealing restorative neuromodulatory effects across behavioral, electrophysiological, and molecular domains.

Together, these findings demonstrate that this TI-TES contact lens provides a pathway-targeted, non-invasive neuromodulation modality while integrating machine-learning-based analytics for robust, multidimensional evaluation of therapeutic efficacy. This approach addresses limitations of previous wearable neuromodulation strategies, providing a versatile platform for the treatment of depression and, potentially, other brain disorders.

RESULTS

Overview of the TI-TES system and therapeutic efficacy evaluation in depression

Figure 1 presents a conceptual overview of our non-invasive TI-TES system for depression therapy along with the validation methods used for efficacy assessment. This system employs a contact lens with integrated electrodes for non-invasive neuromodulation. To realize a mechanically compliant TI-TES contact lens, we designed a microstructured electrode array composed of serpentine interconnects and localized stimulation electrodes (Figure 2A). The serpentine geometry enabled mechanical stretchability while maintaining electrical continuity, thereby ensuring stable operation under lens deformation. To construct transparent and highly flexible electrodes, an ultrathin gallium oxide (GaOx) layer with a thickness of 3 nm was first printed.[37] A Pt layer was then vacuum deposited, followed by additional Pt decoration to further enhance electrical conductivity. Fabrication details for the TI-TES contact lens are described in methods and Figure S1. A schematic cross-sectional view illustrates the layered structure, where a thin Pt layer (1 nm) was deposited on GaOx (3 nm), while Pt nanoclusters, denoted as platinum black (PtB), were selectively coated only on the stimulation electrodes to enhance charge injection capability (Figures 2B and S2). The patterned architecture was well defined, as confirmed by optical microscopy (OM) and scanning electron microscopy (SEM) (Figures 2C and 2D), demonstrating the precise formation of serpentine interconnects and stimulation electrodes. The fabricated electrodes on glass substrates exhibited excellent optical transparency, as shown in Figure 2E, highlighting their suitability for integration into vision-related platforms. Following the molding process, the electrode array was seamlessly embedded within the curved lens without any structural deformation while retaining its high optical clarity (Figure 2F). Optical transmittance spectra confirmed that the device maintained >80% transparency across the visible range, with negligible changes after molding (Figure 2G). Electrochemical modification of the stimulation electrodes with Pt nanoclusters was confirmed by both OM and SEM imaging, showing a clustered morphology with densely distributed nanostructures across the electrode surface (Figure 2H). This modification markedly reduced electrode impedance across a broad frequency range, as demonstrated by electrochemical impedance spectroscopy (Figure 2I). Specifically, pristine Pt-GaOx electrodes exhibited an impedance of 20.3 kΩ at 1 kHz, whereas Pt nanocluster-modified Pt-GaOx electrodes (PtB-Pt-GaOx) showed a markedly reduced impedance of 2.8 kΩ (with an electrode area of 0.0314 mm^2). Concurrently, the charge storage capacity (CSC) increased substantially from 7.17 mC cm^{-2} to 15.60 mC cm^{-2} after Pt nanocluster modification, confirming the improved charge transfer capability (Figure 2J). In addition, the charge injection capacity (CIC), which represents the maximum reversible charge that can be safely delivered during stimulation, was calculated to be 254.6 μC cm^{-2} for the PtB-Pt-GaOx electrodes (Figure 2K). This value is well within the range reported for high-performance neural stimulation electrodes, confirming that the TI-TES electrodes can deliver sufficient charge while maintaining electrochemical safety.[38] Furthermore, accelerated aging tests (12 days at 87°C, which corresponds to 12 months at 37°C) showed minimal impedance change over time (from 2.78 ± 0.01 kΩ to 3.02 ± 0.09 kΩ), validating the system's long-term stability and suitability for sustained stimulation (Figure 2L).

This TES system utilizes TI stimulation. Each electrode pair positioned on the corneal surface delivers a high-frequency electric field at frequencies exceeding 1 kHz. These fields are configured to intersect precisely at the retina, where they interfere to generate a localized, low-frequency envelope wave (Figures S3A and S3B). This TI-mediated approach is critical, as it leverages the principle that high-frequency biases can pass through neural tissue with minimal direct neural activation. However, when two such biases with slightly different frequencies intersect, their interference generates a low-frequency envelope field that effectively modulates neuronal membrane potentials and can trigger action potentials. This mechanism allows for targeted stimulation of deep retinal-brain pathways while minimizing off-target effects on surrounding ocular regions.[31,32,34] To experimentally examine the spatial characteristics of the TI-induced field within the retina, we performed multisite measurements using an epiretinal recording approach. A nine-channel Au epiretinal multielectrode array was fabricated and surgically inserted into the mouse epiretinal region (Figure S4), and the positions of individual channels across the retinal surface were verified using fundus imaging (Figure S5). TI envelope signals evoked by TI-TES stimulation (frequency 20 Hz, peak-to-peak amplitude 200 mV) were then recorded simultaneously from nine retinal locations (Figure S6). The measurements revealed that the peak-to-peak amplitude was maximal at the central retinal region (channel 5), corresponding to the designed interference zone of the TI-TES contact lens (Figure S7A). The peak-to-peak amplitude at this location was closest to the intended 200 mV stimulation level, whereas channels located progressively farther from the center exhibited lower envelope amplitudes. Spatial peak-to-peak amplitude mapping further demonstrated a gradual decrease in TI envelope magnitude from the center toward peripheral retinal regions (Figure S7B). These findings experimentally confirm that the effective stimulation field generated by TI-TES is not uniform but spatially shaped within the retinal volume, with maximal modulation occurring at the designed interference region. This

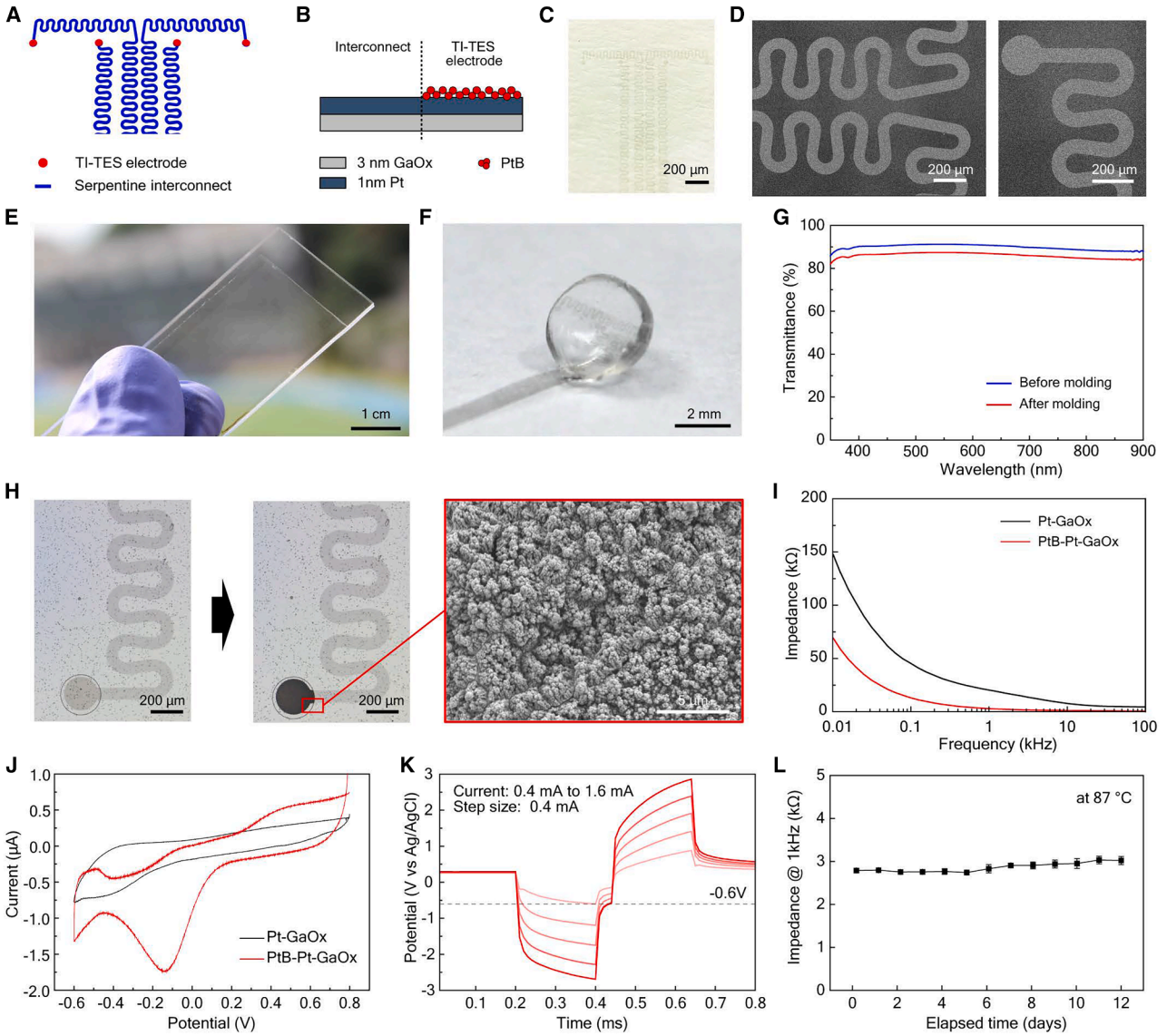

Figure 2. Characterization of the Pt nanocluster-coated electrode

(A) Schematic illustration of the TI-TES electrode.

(B) Cross-sectional schematic showing the layered structure of the electrodes.

(C) Optical microscopy (OM) image of the patterned electrode placed on paper.

(D) Scanning electron microscopy (SEM) images showing the well-defined serpentine interconnects and stimulation electrodes. Scale bars, 200 μm.

(E) Photograph of a fabricated transparent TI-TES electrode on a glass substrate. Scale bar, 1 cm.

(F) Photograph of the TI-TES lens. Scale bar, 2 mm.

(G) Optical transmittance spectra of the TI-TES electrode before (blue) and after (red) molding.

(H) OM (left) and SEM (right) images of stimulation electrodes after Pt nanocluster deposition, showing clustered nanostructures. Scale bars, 200 μm (OM) and 5 μm (SEM).

(I) Electrochemical impedance spectroscopy of pristine Pt-GaOx electrodes (black) and PtB-Pt-GaOx electrodes (red).

(J) Representative cyclic voltammetry curves comparing the charge storage capacity (CSC) of Pt-GaOx and PtB-Pt-GaOx electrodes.

(K) Representative voltage transients used to determine the charge injection capacity (CIC) of PtB-Pt-GaOx electrodes.

(L) Accelerated aging test of PtB-Pt-GaOx electrodes conducted at 87°C (equivalent to 12 months at 37°C). The data are presented as mean ± SD.

supports the targeted neuromodulation capability of the TI-TES approach and distinguishes it from conventional low-frequency stimulation, which primarily activates tissue near the electrode interface.

We assessed the safety of the TI-TES system by evaluating its potential adverse effects on ocular tissues. For these experiments, C57BL/6 mice were used instead of rd1 mice, as this strain possesses normal retinal anatomy and is therefore

appropriate for reliable evaluation of ocular tissue integrity. The animals were divided into a TES-off group (no stimulation) and a TES-on group following TI-TES treatment. TI-TES was applied using the optimized stimulation protocol established in this study: two high-frequency signals (2,000 Hz and 2,020 Hz) were combined to generate a 20-Hz temporal interference envelope (peak-to-peak amplitude 200 mV) for 30 min per day over a 3-week treatment period. First, corneal safety was examined. Histological analysis (H&E staining) showed no structural abnormalities, and corneal thickness did not differ between the TES-on and TES-off groups (Figure S8). To further assess cellular damage and inflammatory responses, immunofluorescence analyses for TUNEL and CD45 were performed. TUNEL staining, which detects DNA fragmentation associated with apoptotic cell death, revealed only minimal signal in both groups (Figure S9A). CD45 staining, a pan-leukocyte marker indicative of inflammatory immune cell infiltration, also showed no detectable increase following stimulation (Figure S9B). Next, retinal safety was evaluated. H&E staining revealed preserved laminar organization and no change in total retinal thickness following TI-TES treatment (Figure S10). Retinal immunofluorescence analyses, including TUNEL staining and microglial activation assessed by Iba1 immunostaining, showed no increase in apoptosis or neuroinflammatory response. Specifically, TUNEL labeling demonstrated the absence of stimulation-induced retinal cell death (Figure S11A), while Iba1 staining, a marker of activated microglia associated with retinal neuroinflammation, showed no elevation in microglial activation (Figure S11B). Taken together, these findings demonstrate that TI-TES delivered through the contact lens does not cause detectable structural damage, apoptosis, or inflammatory activation in ocular tissues and is biocompatible during long-term application.

To further examine the broader effects of TI-TES on the ocular environment, intraocular pressure (IOP) was measured before, during, and after the treatment period. No significant alterations in IOP were observed, confirming that TI-TES did not adversely affect ocular homeostasis (Figure S12). Biocompatibility with human corneal epithelial cells (HCE-2) was also confirmed. A live/dead assay showed no evidence of dead cells, and the CCK-8 assay indicated a cell viability of 99.25% ± 5.82%, indicating no significant cytotoxicity compared to the control group (Figure S13). These results collectively demonstrate that the TI-TES system is safe and stable, showing no adverse effects during the treatment period.

Figure 1 also illustrates the activation of the eye-brain connection via TI-TES. The TI-TES-generated low-frequency envelope waves at the retina stimulate both retinal ganglion cells (RGCs) and intrinsically photosensitive RGCs (ipRGCs). This stimulation activates two distinct neuroanatomical pathways that connect the eye to the brain, leading to neuromodulation in brain regions associated with depression, such as the HPC and PFC.[25,39] The detailed RGC and ipRGC neural pathways are presented in Note S1. To provide direct functional evidence that TI-TES engages the RGC pathway, we performed *in vivo* epiretinal recordings during TI-TES application. The TI-TES contact lens was placed on the cornea, and stimulation was delivered with optimized parameters established in this study (Figure S14). At the same time, a recording electrode was inserted into the retina in an epiretinal configuration to directly record retinal neural activity originating from RGCs. As shown in Figure S15, raw epiretinal traces exhibit clear spike events that emerge immediately following TI-TES application, whereas only sparse spontaneous activity is observed during the prestimulation baseline period. A raster plot shows a pronounced clustering of spike events around the TI-TES time window. Consistently, spike-count histograms reveal a marked increase in the number of detected spikes shortly after TI-TES compared to baseline. These stimulation-evoked spike responses indicate that TI-TES induces action-potential firing in RGCs, including ipRGCs, rather than producing only subthreshold or localized retinal effects. To further determine whether TI-TES-evoked retinal activation propagates to the brain along the RGC pathway, we measured visual evoked potentials (VEPs) from the visual cortex before and after TI-TES. TI-TES was applied through the contact lens on the cornea, while an active recording electrode for VEPs was positioned in the visual cortex at a standard location (Figures S16A and S16B). This experimental configuration enabled direct assessment of whether stimulation delivered at the eye produces measurable changes in cortical responses, thereby reflecting signal transmission from the retina to the brain. The representative VEP waveform shown in Figure S16C highlights the characteristic negative (N1) and positive (P1) components of the cortical visual response.[40] In particular, the N1 peak reflects early cortical activation driven by retinal input along the RGC pathway and is widely used as a quantitative marker of visual signal transmission from the retina to the visual cortex. VEP waveforms were first recorded under baseline conditions prior to TI-TES and then recorded again after TI-TES using the same stimulation and recording parameters. Before TI-TES, cortical signals remained close to baseline with no clear VEP components (Figure S17A). In contrast, following TI-TES, VEP waveforms exhibited a clear canonical pattern characterized by a pronounced negative deflection followed by a positive deflection, corresponding to the N1 and P1 components (Figure S17B). To quantitatively evaluate this change, we measured the N1 amplitude at 50 ms. The post-TI-TES condition showed a marked increase in N1 amplitude compared to the prestimulation baseline (Figure S17C), indicating a strong enhancement of cortical VEP responses following TI-TES. Taken together, the epiretinal recording and VEP results provide converging electrophysiological evidence that TI-TES engages functional RGC-mediated pathways from the retina to the brain. The observation of stimulation-evoked action-potential firing in RGCs demonstrates that TI-TES directly activates retinal output neurons, while the enhanced cortical VEP responses confirm that this retinal activation is effectively transmitted to downstream brain regions. These findings support the conclusion that TI-TES modulates brain activity through established RGC- and ipRGC-associated eye-brain circuits.

The therapeutic effects observed in this study, including restored brain connectivity, increased neurotrophic factors, and reduced inflammation associated with depression, were rigorously validated through a multidomain assessment framework encompassing behavioral, neural, and biological analyses. Notably, all primary therapeutic efficacy experiments were conducted in rd1 mice, which exhibit photoreceptor degeneration. This experimental choice was intentional. Because TI-TES

engages retina-brain pathways, including both image-forming and non-image-forming circuits, we sought to eliminate photoreceptor-driven visual input as a potential confounding variable. By using rd1 mice, we ensured that the observed behavioral and neurobiological improvements could not be attributed to altered visual perception or visually mediated environmental cues, thereby isolating the contribution of direct retinal output neuron activation to downstream neuromodulation.

In addition, we employed a machine-learning approach to integrate and classify the comprehensive dataset, providing a robust, multidimensional validation of the TI-TES system's efficacy. The TES-treated mouse group was consistently classified with the sham group and clearly separated from the depression group, underscoring the ability of TI-TES to reverse depression-related biomarkers effectively.

Optimization of TI-TES parameters and behavioral efficacy assessment

Behavioral analysis provides a primary and intuitive measure of depression severity in animal models. The mice were divided into three groups: a sham group, a corticosterone-induced depression-like (Dep) group, and a TI-TES-treated Dep group (TES). Details of the model preparation are provided in Note S2. To evaluate the therapeutic effects of TI-TES, we conducted standard individual behavioral tests, including the open-field test (OFT), tail-suspension test (TST), forced swim test (FST), social behavioral test, and three-chamber test (Figure 3A). We first optimized the TI-TES parameters by assessing time spent in the center zone of the OFT. For parameter screening across multiple stimulation conditions, a single sensitive and low-variance behavioral metric was selected to enable stable and reproducible comparisons. The OFT provides a continuous readout with minimal influence from task-specific stress, fatigue, or learning effects, making it well suited for repeated measurements. In contrast, other behavioral assays may introduce additional variability under repeated testing conditions. To avoid bias from composite scoring schemes and potential overfitting, integrated behavioral indices were not used at this stage and were instead reserved for evaluating the overall therapeutic effects after parameter optimization. Future studies may incorporate additional behavioral metrics or composite indices during the optimization process to further refine this approach. TI stimulation was used to generate envelope signals with frequencies of 10, 20, or 30 Hz, produced by pairing a 2,000-Hz carrier with secondary frequencies of 2,010, 2,020, or 2,030 Hz, respectively, and peak-to-peak envelope amplitudes of 50, 100, 200, or 400 mV. The stimulation durations were set to 10, 30, or 50 min. The highest OFT score, defined as the time spent in the center zone, was achieved with a 20-Hz frequency, 200-mV peak-to-peak amplitude, and 30-min duration (Figure 3B). This optimal setting was then applied for up to 4 weeks to determine the most effective treatment period. The results showed that 3 weeks of treatment were sufficient to achieve a significant therapeutic effect, and this was chosen as the standard treatment period (a frequency of 20 Hz, a peak-to-peak amplitude of 200 mV, and a duration of 30 min per day for 3 weeks) for all subsequent experiments (Figure 3C).

In the OFT test, the Dep group showed reduced locomotor activity (measured by traveled distance) and increased anxiety levels (measured by time in center zone). Over the 10-min observation, the TES group demonstrated a 76% increase in traveled distance (Figures 2D and 2E) and a 132% increase in time spent in the center zone (Figure 3F) compared to the Dep group. Similarly, in the TST and FST, which measure helplessness, the Dep group showed significantly higher immobility. TI-TES treatment reduced immobility by 48% in the TST (Figures 3G and 3H) and 45% in the FST (Figures 3I and 3J), indicating a reversal of depressive behavior. The three-chamber test is a widely used behavioral assay designed to evaluate social preference and social novelty in rodents (Figure 3K).[41,42] Details of the three-chamber test procedure are provided in Note S3. This test revealed that the Dep group exhibited reduced social interaction, whereas the TES group showed a significant improvement in social preference and novelty indices, approaching the levels of the sham group (Figures 3L and 3M). These results collectively and robustly confirm that the TI-TES treatment effectively alleviates depressive behaviors in mice.

To evaluate whether these antidepressant-like effects were dependent on photoreceptor degeneration, we conducted additional validation experiments in wild-type C57BL/6 mice with intact visual systems. Using the same corticosterone-induced depression model and TI-TES protocol, behavioral assessment was performed using the OFT (time in center zone). As shown in Figure S18, TI-TES treatment significantly increased time spent in the center zone relative to the Dep group, restoring behavioral performance toward sham levels. These results demonstrate that TI-TES-induced antidepressant-like effects are reproducible in animals with intact photoreceptor function and are not dependent on retinal degeneration.

To further examine whether the therapeutic effects of TI-TES are mediated through the RGC- and ipRGC-associated pathways, we next performed a pathway-disruption experiment using intravitreal *N*-methyl-D-aspartic acid (NMDA) injection to ablate RGCs. NMDA injection, a well-established method for inducing excitotoxic degeneration of RGCs, resulted in a marked reduction in the number of cell nuclei within the ganglion cell layer (GCL), confirming effective RGC ablation (Figure S19).[43,44] Following confirmation of RGC loss, TI-TES was applied using the same stimulation parameters as in the behavioral experiments described above. Therapeutic outcomes were then evaluated using the OFT, with time spent in the center zone used as the primary quantitative metric of depression-like behavior. As described above, in mice that did not receive NMDA injection (TI-TES group), TI-TES significantly increased time spent in the center zone. In contrast, this behavioral improvement was not observed in NMDA-treated mice (NMDA + TES group) (Figure S20), indicating that disruption of RGC pathways abolishes the therapeutic efficacy of TI-TES. These results demonstrate that intact RGC-dependent downstream pathways are required for TI-TES-induced behavioral improvement.

To place the behavioral efficacy of TI-TES in the context of an established pharmacological treatment, we additionally included a fluoxetine-treated group as a reference antidepressant control. Fluoxetine is a selective serotonin reuptake inhibitor widely used

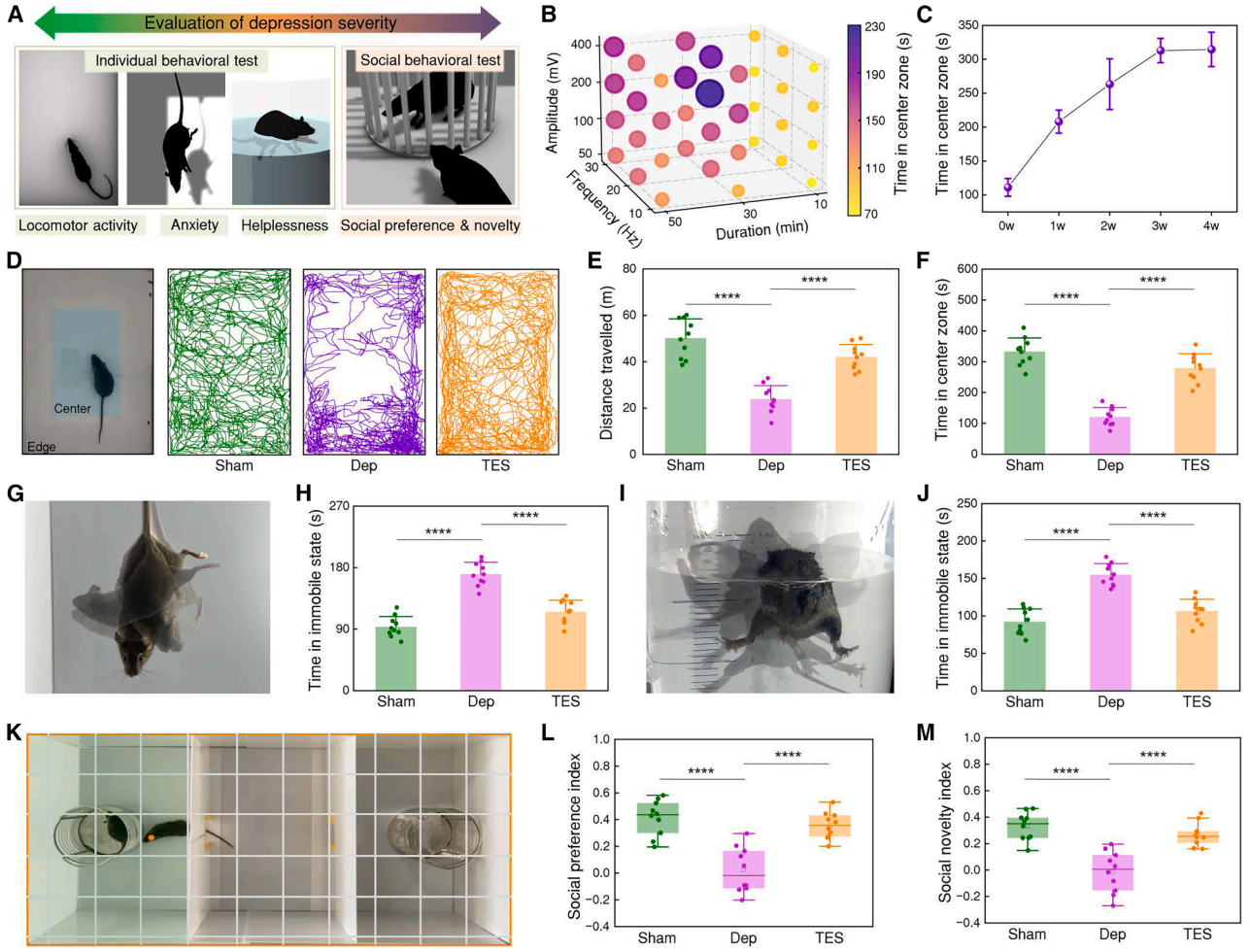

Figure 3. Optimization of TI-TES parameters and behavioral evaluation across sham, depression, and TI-TES-treated mouse models

(A) Overview of behavioral tests conducted to evaluate depression severity in mice.

(B) 3D scatterplot showing OFT scores (time in center zone) across 36 TES stimulation conditions. Parameters varied by frequency (10, 20, and 30 Hz), peak-to-peak amplitude (50, 100, 200, and 400 mV), and duration (10, 30, and 50 min).

(C) Weekly OFT scores under the optimized TES condition (20 Hz, 200 mV, 30 min/day) over 4 weeks of treatment. Data represent the mean ± SD (n = 5, biologically independent mice model of depression).

(D) Representative tracking paths of mice from the OFT in sham, Dep, and TES groups.

(E and F) Quantification of locomotor activity in the OFT, including total distance traveled (E) and time spent in the center zone (F) across sham, Dep, and TES groups.

(G) Image of the TST setup.

(H) Immobility time measured in the TST.

(I) Image of the FST setup.

(J) Immobility time measured in the FST.

(K) Setup of the three-chamber test for assessing social preference and novelty.

(L and M) Quantification of social interaction behavior from the three-chamber test, including the social preference index (L) and social novelty index (M) (n = 10 for each group).

All data in graphs are presented as mean ± SD. Statistical comparisons were performed using unpaired, one-sided t tests with Holm-Bonferroni correction; ****$p < 0.0001$. In boxplots presented in (L) and (M), data are presented as median with interquartile range (IQR), with individual data points overlaid.

in both clinical practice and preclinical depression models and is commonly employed as a benchmark for antidepressant efficacy.[45] In this study, fluoxetine was administered by daily subcutaneous injection (20 mg kg^{-1}) for 3 consecutive weeks, following the same experimental timeline and behavioral assessment schedule as the TI-TES treatment. Behavioral outcomes were compared across four groups: sham, Dep, Dep + TI-TES, and Dep + fluoxetine. In the OFT, fluoxetine treatment significantly increased time spent in the center zone compared to the Dep group, indicating reduced anxiety- and depression-like behavior. Notably, the TI-TES group exhibited a comparable increase in center-zone time, reaching levels similar to those

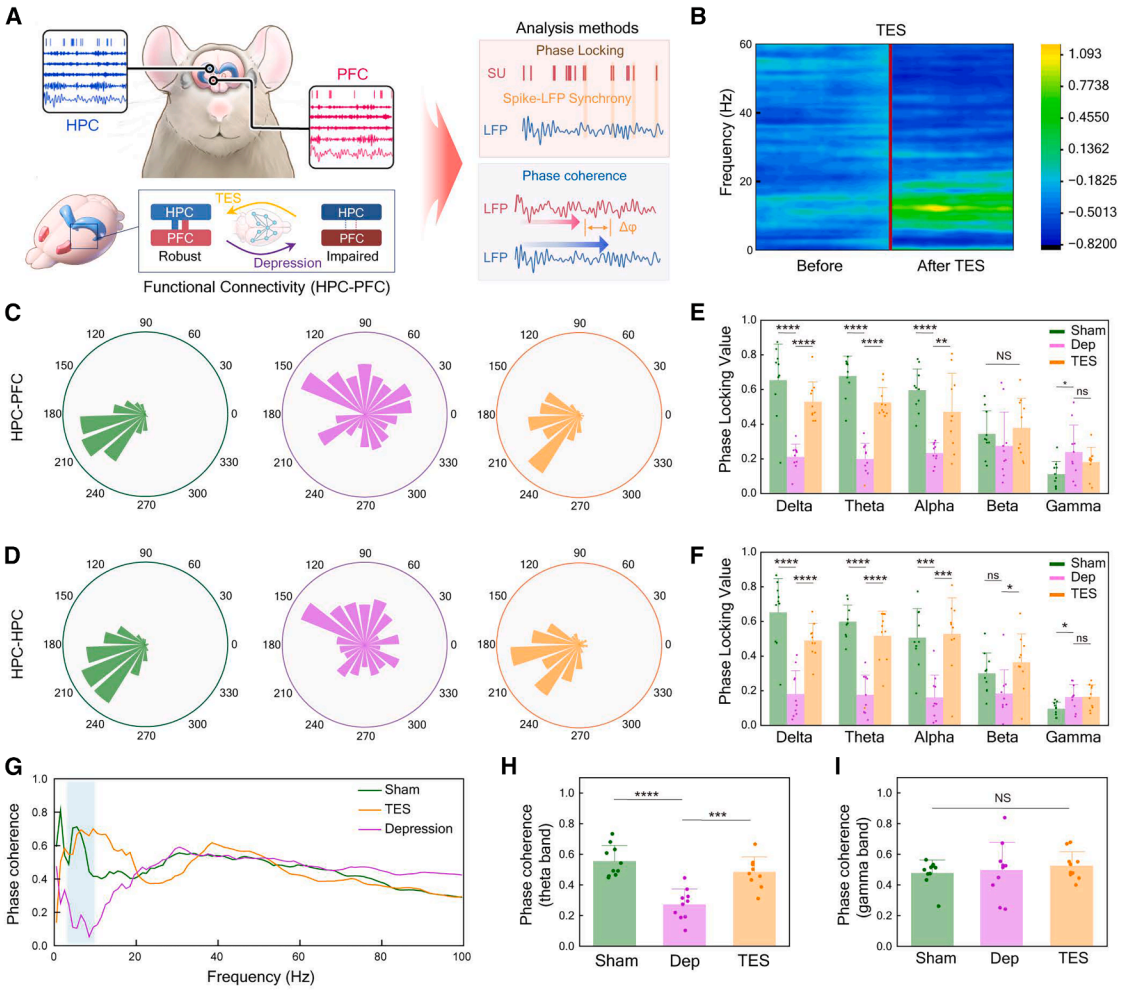

Figure 4. Neural signal recording and analyses

(A) Schematic diagram of neural signal recording and analyses. Neural probes were inserted into the HPC and PFC to record SU and LFP signals.

(B) Representative power spectrum analysis showing changes in neural oscillations before and after TES.

(C and D) Rose plots of phase-locking results between HPC-PFC (C) and HPC-HPC (D) in sham, Dep, and TES groups (n = 10 mice per group). Green, purple, and orange represent the sham, Dep, and TES groups, respectively.

(E and F) Quantified phase-locking values across five frequency bands (delta, theta, alpha, beta, and gamma) for HPC-PFC (E) and HPC-HPC (F) regions.

(G) Representative phase-coherence spectra of the three groups. Delta and theta frequency ranges, where the discrepancies are most pronounced, are highlighted in blue.

(H and I) Phase-coherence values in the theta (H) and gamma (I) bands (n = 10 mice per group).

All data in bar graphs are presented as mean ± SD. Statistical comparisons were performed using unpaired, one-sided t tests with Holm-Bonferroni correction. ns, $p > 0.05$ (not significant); *$p < 0.05$, **$p < 0.01$, ***$p < 0.001$, and ****$p < 0.0001$. NS indicates no significance by one-way ANOVA.

observed in the fluoxetine-treated group (Figure S21A). Consistent trends were observed in the TST and FST, which assess behavioral despair. While the Dep group showed significantly increased immobility, both fluoxetine and TI-TES treatments markedly reduced immobility times in these assays (Figures S21B and S21C). Across all three behavioral paradigms, the magnitude of improvement induced by TI-TES was comparable to that achieved with fluoxetine treatment. These results demonstrate that the antidepressant-like effects of TI-TES are comparable to those of a widely used pharmacological treatment across multiple, well-established behavioral assays, providing a direct benchmark for estimating the relative therapeutic efficacy of the proposed neuromodulation strategy.

Neural signal analysis for assessing TI-TES effects on brain functional connectivity

Depression is known to disrupt not only single brain regions but also the functional connectivity between brain regions, particularly between the HPC and PFC.[46–49] To investigate the effects of TI-TES on this connectivity, we simultaneously recorded neural signals from the HPC and PFC of mice using implanted probes (Figures 4A and S22). To ensure the accurate evaluation

of the effects of TES on neural circuitry, it is essential to minimize tissue damage caused by implanted neural probes and thereby preserve the integrity of neural signal recordings. To this end, we fabricated neural probes using materials with softness comparable to that of brain tissue. Specifically, a fluorinated elastomer (Axoft, USA) was employed as the encapsulation material owing to its mechanical compliance with neural tissue, biocompatibility that reduces chronic immune response, long-term stability in physiological environments, and compatibility with microfabrication processes enabling precise patterning (Figure S23A).[50] Following the patterning of the fluorinated elastomer bottom layer, liquid metal (EGaIn; 75.5 wt % gallium, 24.5 wt % indium) was directly printed (Figure S23B). Subsequently, the fluorinated elastomer top layer was coated, and the recording sites were exposed (Figure S24A). Pt nanoclusters were then deposited onto the exposed recording areas to enhance the electrochemical surface properties (Figure S24B). The deposition of Pt nanoclusters substantially reduced impedance as a result of the enlarged electrochemical surface area induced by the nanostructures. Figure S24C presents the impedance spectroscopy comparing Pt-nanocluster-coated liquid metal (PtB-EGaIn) and pristine EGaIn. At 1 kHz, PtB-EGaIn exhibited an impedance of 209.2 kΩ, which is approximately five times lower than that of pristine EGaIn (1,103.6 kΩ). Detailed fabrication/implantation procedures and setup for neural recording are described in the methods section. The recorded signals were separated into local field potentials (LFPs) and single-unit potentials (SUs) by bandpass filtering. The LFPs were further filtered into five distinct frequency bands—delta (0.5–4 Hz), theta (4–8 Hz), alpha (8–12 Hz), beta (12–28 Hz), and gamma (28–100 Hz)—and spikes were sorted from the SUs. The signals were analyzed for changes in power spectrum and functional connectivity on the depression-like mouse model. As shown in Figure 4B, short-term TI-TES application modulated neural oscillations, particularly in the low-frequency bands (0–20 Hz). The average spectral power before and after the TI-TES treatment is also shown in Figure S25. These findings indicate that TI-TES exerts a restorative effect on depression by promoting the recovery of impaired neuronal functional connectivity, as evidenced by increased neural power. This observation aligns with previous reports suggesting that depression is closely associated with abnormalities in the low-frequency band of neural signals and that electrical stimulation alleviates these neural dysfunctions to restore functional connectivity.[51,52]

Beyond short-term spectral changes, we conducted phase-locking and phase-coherence analyses to quantify long-term changes in synchronization between HPC and PFC. Our analysis focused on the theta band, as it is a major medium for inter-regional communication between the HPC and PFC. In phase-locking analysis, we assessed the synchronization between LFP and SU spikes within and between regions (HPC-PFC and HPC-HPC). This analysis identifies instances where an SU spike is aligned to a specific phase of the LFP, thereby providing insight into the functional coupling of distinct brain regions. We recorded and counted these occurrences from ten mice in each group, and the results were visualized using rose plots with the number of counts and the corresponding phase as the axes (Figures 4C and 4D). This analysis provided insight into how well neuronal firing was temporally aligned with ongoing oscillations in connected brain regions, serving as an indicator of functional coupling between distinct brain regions. The strength of locking was evident from the clustering of spikes. We used Rayleigh's test to calculate a p value for each instance, where a lower p value indicated a stronger locking.[53] The phase-locking value (PLV), a quantitative measure of phase locking, was also plotted (Figures 4E and 4F).

Consistent with the importance of the theta band, the TES group exhibited notably higher PLVs than the Dep group for both HPC-PFC and HPC-HPC, with increases of 163.6% and 192.6%, respectively. We also observed an ascending trend from the Dep group to the TES group in the delta and alpha bands. For HPC-PFC, the delta band showed a 150.8% rise and the alpha band a 102.1% rise. In contrast, the beta band showed only a 38.3% increase, and the gamma band showed a 24.6% decrease. A similar pattern was seen in HPC-HPC: the delta band showed a 172.2% increase and the alpha band a 227.3% increase, while the beta band had a 97.7% increase and the gamma band only a 1.1% increase. These significant changes in the delta and alpha bands are consistent with prior studies.[54–56] Statistical significance of the PLVs from these bands was verified by t tests, as shown by the asterisks on the graphs. The average Rayleigh's p values for each group across all five bands were also plotted (Figure S26). All three components of this analysis (rose plots, PLVs, and Rayleigh's p values) showed a consistent trend: the sham group exhibited the strongest locking, the Dep group significantly lower values, and the TES group values that were higher than the Dep group and closer to the sham group. These results indicate that TI-TES treatment effectively restored neural synchronization within the HPC and between the HPC and PFC.

In phase-coherence analysis between LFP bands of different regions (HPC-PFC), we determined the degree of synchronization between the signals. Phase coherence measures the consistency of the phase relationship, thereby reflecting functional connectivity between distinct brain regions.[57] The representative plot in Figure 4G shows significant differences among the three groups, particularly in the theta band, where the Dep group exhibited the lowest coherence. The TES and sham groups, in contrast, showed similarly high levels of coherence. As shown in Figure 4H, the TES group had a 77.8% greater average coherence value than the Dep group. This finding is consistent with the phase-locking results, indicating that TI-TES treatment reversed the functional connectivity impairments associated with the depressive state, restoring connectivity to levels closer to the sham group. The coherence values in the gamma band showed no pronounced differences among the three groups (Figure 4I). These findings are consistent with prior studies reporting that depression-related neural alterations are most evident in the theta band.[47,54,58]

Overall, the results demonstrate the therapeutic potential of TI-TES in modulating functional connectivity within and between the HPC and PFC. The robust phase locking and high coherence values seen in the TI-TES group are hallmarks of a healthy neural state, as evidenced by the difference between the sham and Dep groups. Therefore, while these results confirm that neural connectivity is disrupted by depression,[33,58] they also verify the

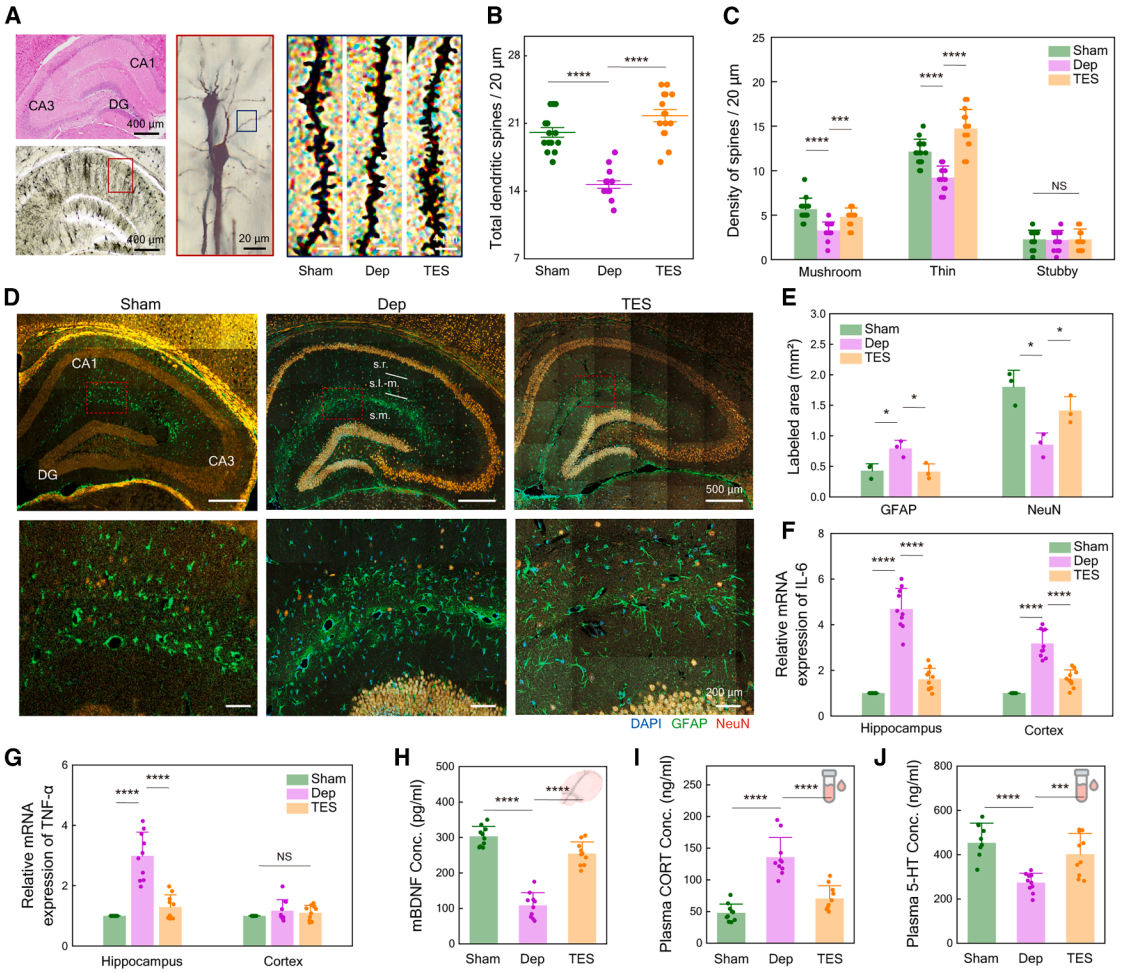

Figure 5. Comprehensive biological assessment of TI-TES efficacy in a mouse model

(A) Representative images of hippocampal sections stained with H&E (top left), Golgi stain (bottom left), and high-magnification views of dendritic spines across sham, Dep, and TES groups (right).

(B) Quantification of total dendritic spine density per 20 μm in each group ($n = 5$ mice per group, three measurements per mouse; total of 15 data points per group).

(C) Subtype-specific dendritic spine densities, including mushroom, thin, and stubby spines.

(D) Representative immunohistochemistry images of hippocampal sections stained for NeuN (orange), GFAP (green), and DAPI (blue). Top: overview of the hippocampus; bottom: magnified CA1 region. DG, dentate gyrus; s.r., stratum radiatum; s.l.-m., stratum lacunosum-moleculare; and s.m., stratum moleculare.

(E) Quantification of labeled areas for GFAP and NeuN markers across groups ($n = 3$ mice per group).

(F and G) Relative mRNA expression levels of IL-6 (F) and TNF-α (G) in the hippocampus and cortex, measured by RT-qPCR ($n = 10$ mice per group).

(H) Mature BDNF (mBDNF) concentrations of all three groups in hippocampal tissue measured by ELISA.

(I and J) Plasma concentrations of corticosterone (I) and serotonin (5-HT) (J) measured by ELISA ($n = 10$ mice per group).

All data in bar graphs are presented as mean ± SD. Statistical comparisons were performed using unpaired, one-sided *t* tests with Holm-Bonferroni correction. ns, $p > 0.05$ (not significant); *$p < 0.05$, **$p < 0.01$, ***$p < 0.001$, and ****$p < 0.0001$. NS indicates no significance by one-way ANOVA.

capability of TI-TES to counteract such disruption to restore connectivity.

Comprehensive biological analysis to assess TI-TES therapeutic effects

To systematically investigate the therapeutic potential of TI-TES, we designed a series of biological experiments that integrated morphological, transcriptional, and biochemical analyses to thoroughly assess the underlying mechanisms of its efficacy. We first explored the effects of TI-TES on neural morphology, as dendritic and synaptic deficits are a core feature of depression pathophysiology.[59] We used the FD Rapid GolgiStain Kit (FD NeuroTechnologies, USA) to analyze dendritic spine morphology in hippocampal neurons, which revealed a strong pattern of Golgi-positive dendritic spines (Figure 5A, middle panel). Detailed protocols are provided in the methods section. The spine morphology for each group is presented in Figure 5A (right panel). As shown in Figure 5B, the total dendritic spine density was reduced in the Dep group compared to the sham group, indicating decreased synaptic connectivity associated with depressive states. In contrast, TI-TES treatment significantly restored dendritic morphology, reflected in a 48.6% recovery

in total spine density relative to the Dep group. Furthermore, we assessed synaptic plasticity by classifying dendritic spines into three morphological types: mushroom, thin, and stubby (Note S4).[60] The Dep group showed a significant reduction in both mushroom and thin spine density (Figure 5C) compared to the sham group, suggesting a global impairment in synaptic plasticity. TI-TES treatment effectively reversed these depressive-induced synaptic deficits, with mushroom spine density recovering by 46.9% and thin spine density increasing by 60.1% relative to the Dep group. No significant differences were observed in the spine density of stubby-shaped spines. These results demonstrate that TI-TES treatment not only mitigates the loss of mature synapses but also supports synaptic plasticity by promoting both stable and dynamic synaptic connections.

The pro-inflammatory cytokines, such as interleukin-6 (IL-6) and tumor necrosis factor alpha (TNF-α), are deeply associated with depressive disorder and psychological stress. Activated astrocytes play a significant role in neuronal degeneration by producing pro-inflammatory cytokines.[61,62] To examine the anti-inflammatory effects of TI-TES, we used immunohistochemistry to investigate the expression of neuronal nuclei (NeuN)-positive neurons and glial fibrillary acidic protein (GFAP)-positive glial cells in the HPC. The coronal section of the HPC was stained with anti-NeuN, GFAP, and 4′,6-diamidino-2-phenylindole (DAPI) (Figure 5D). Following depression induction, GFAP protein levels, a marker for astrocyte activation, significantly increased by 85.5% relative to the sham group (Figure 5E). In contrast, TI-TES effectively mitigated this activation, reducing GFAP-labeled regions by 48.1% compared to the Dep group. Additionally, the viability of hippocampal neurons (NeuN-positive cells) decreased by 52.6% in the Dep group relative to the sham group, and this loss was partially restored by TI-TES treatment, which achieved a 65.5% recovery relative to the Dep group. These results collectively demonstrated that TI-TES mitigates glial activation and protects neuronal integrity in the depression-affected hippocampal region.

To further quantify the inflammatory response and other key biological markers, we conducted a series of transcriptional and biochemical analyses. Using RT-qPCR, we measured the relative mRNA expression levels of two key pro-inflammatory cytokines, IL-6 and TNF-α. In the HPC, the Dep group exhibited a marked upregulation of both IL-6 and TNF-α compared to the sham group (Figures 5F and 5G). TI-TES significantly alleviated this inflammation, reducing IL-6 and TNF-α levels by 65.8% and 56.8%, respectively. While IL-6 expression in the cortex was similarly elevated and reduced by TI-TES (48.5% decrease), TNF-α expression showed no significant differences across groups in the cortex, possibly due to regional heterogeneity in inflammatory responses.[63,64] We also measured the levels of brain-derived neurotrophic factor (BDNF), a crucial regulator of synaptic plasticity and neurogenesis.[65,66] As shown in Figure 5H, depression led to a significant 64.2% reduction in mature BDNF (mBDNF) levels in the HPC. TI-TES treatment robustly restored mBDNF levels, achieving a remarkable 131.1% recovery relative to the Dep group, suggesting enhanced neurotrophic signaling. Furthermore, we assessed systemic stress markers. Depression induction with corticosterone resulted in elevated plasma corticosterone concentration and decreased serotonin (5-HT) levels. As shown in Figures 5I and 5J, TI-TES treatment effectively normalized these markers: it reduced plasma corticosterone levels by 48.1% and restored 5-HT levels, achieving a 46.9% recovery relative to the Dep group.

Our integrated morphological, immunohistochemical, transcriptional, and biochemical findings provide compelling evidence that TI-TES exerts a multifaceted therapeutic effect, encompassing the restoration of synaptic integrity and plasticity, the suppression of neuroinflammation, and the normalization of key neurotrophic and systemic stress markers.

Machine-learning-based group classification for efficacy assessment

To provide a comprehensive, holistic assessment of TI-TES efficacy, we developed an integrated machine-learning framework using a support vector machine (SVM) classifier to classify the three groups (sham, Dep, and TES, $n = 10$ for each group) based on behavioral, neural, and biological data (Figure 6A).[67,68] Classification with an SVM necessitates preprocessing for efficient training, especially considering the heterogeneity in various aspects of our data such as the scales and proportionality.[69] Here, an SVM was employed to classify depression-like and normal-like states based on integrated behavioral, neural, and biological features, and to determine whether TI-TES-treated animals were positioned closer to the depression or sham group in the multidimensional feature space. Thus, the SVM served as an objective tool to evaluate system-level recovery rather than to infer causal mechanisms.

As a preliminary and purely exploratory step, we used t-distributed stochastic neighbor embedding (t-SNE), projecting high-dimensional data into a two-dimensional (2D) space in an unsupervised manner (Figure 6B).[70] This visualization illustrates that samples from the depression group tend to occupy a different region of the 2D space, while the TES and sham groups appear intermingled.

To investigate inter-factor relationships, we conducted a series of correlation analyses across all features collected from behavioral, neural, and biological assessments. Although the p value quantifies evidence against null hypothesis, handling a large number of correlations increases the risk of chance findings. Therefore, the Benjamini-Hochberg false discovery rate (FDR) correction was applied to control for multiple testing. FDR correction was applied separately to Pearson and Spearman correlation coefficients. Moreover, a partial correlation analysis controlling for experimental group was conducted to assess the influence of potential covariates. After adjusting for group effects, most of the correlations were no longer statistically significant. This suggests that the observed correlations were largely driven by differences between groups among the sham, Dep, and TES conditions, rather than within-group associations. A chord diagram was constructed based on the Pearson correlation coefficient of the resulting pairs (Figure 6C). An enlarged version of the chord diagram and the list of correlation coefficients and p values with FDR correction (q values) are provided in Figure S27. This series of analyses served as part of our data preprocessing, providing insights into how factors from different domains interact. Notably, behavioral features showed

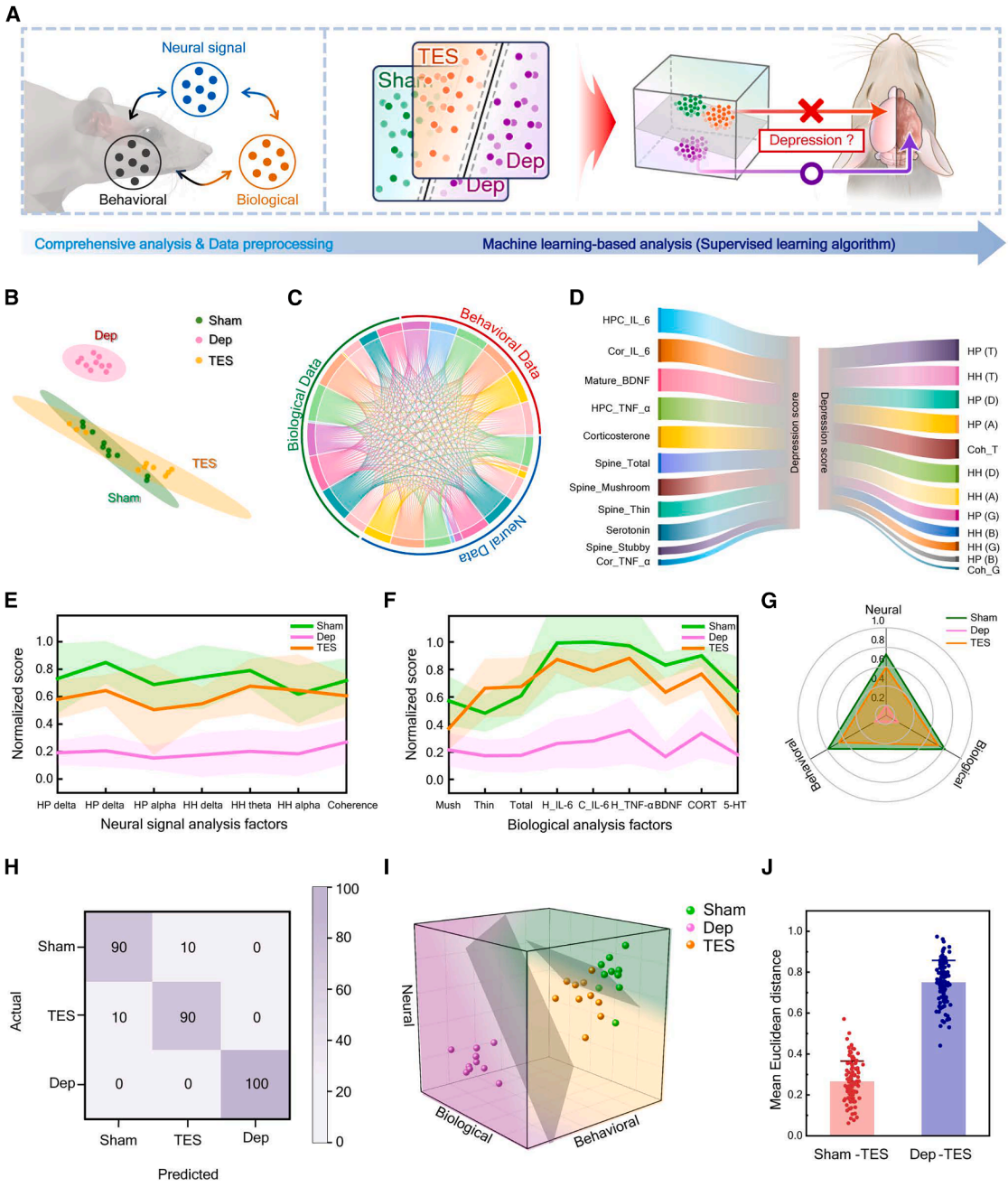

Figure 6. Machine-learning analyses

(A) Schematic showing the flow of the machine-learning analyses.

(B) t-SNE plot from the collected data, visualizing spatial distribution of the samples of the three groups. Perplexity: 5; learning rate: 200; initialization: PCA; random seed = 42.

(C) Chord diagram showing the relative correlations between all factors.

(D) Sankey diagram showing the relevance of each feature in biological and neural data with respect to the depression score.

(E and F) Normalized scores of each factor in (E) neural signal and (F) biological data.

(G) Rose plot showing scores of all three groups.

(H) Confusion matrix of the support vector machine classifier demonstrating the classification accuracy for predicting Dep, sham, and TES groups in a test set. The SVM classifier was trained based on scores from all three analyses and was used to predict the class of each model through a 5-fold cross-validation procedure.

(I) Support vector machine-assisted data classification. Two hyperplanes were computed to separate Dep, TES, and sham groups.

(J) Mean Euclidean distances between the three groups. Data are presented as mean ± SD.

strong and consistent correlations with both neural and biological domains, suggesting their suitability as a reference point. Based on these results, behavioral data were normalized and used to define a "depression score" that reflects the progression toward a depressive state. The normalized scores of behavioral factors are shown in Figure S28. The *p* values between this score and each neural or biological factor were then calculated and visualized using a Sankey diagram (Figure 6D). Factors with minimal contribution included stubby spine density, cortical TNF-α, gamma-band coherence, and beta-band phase locking. Application of FDR revealed high *q* values for the five features, as shown in Figure S29. Therefore, these features were discarded for the subsequent analyses, and the remaining dataset was normalized for supervised machine learning. Normalization was important as multiple data modalities were concatenated, which could cause dominance of one modality. A detailed explanation of min-max scaling is included in methods. The resulting normalized values of the neural and biological factors are presented in Figures 6E and 6F, respectively. The normalized values of behavioral factors are shown in Figure S30. These plots demonstrate a clear separation between the sham and Dep groups, with the TES group trending toward the sham group, further supporting the therapeutic effect. To visualize multivariate relationships and to intuitively compare the relative contributions of each data domain, a rose plot was generated to represent the proportional influence of neural, behavioral, and biological factors across groups (Figure 6G). In this plot, the TES group closely resembled the sham group, indicating that TI-TES treatment restored the overall profile toward a healthy state.

Finally, we applied a supervised learning approach using an SVM classifier trained on the refined feature set. Classification performance was evaluated using a confusion matrix across the three groups, which confirmed accurate group discrimination (Figure 6H). To prevent data leakage due to repeated measures, stratified 5-fold cross-validation was performed with grouping at the animal level, ensuring that all samples from the same animal were assigned exclusively to either the training set or test set within each fold. For visualization, all data points were placed in a three-dimensional (3D) space defined by neural, biological, and behavioral scores. Linear decision boundaries derived from the trained three-class SVM frameworks were then projected onto this space to illustrate the separation between Dep, TES, and sham groups (Figure 6I). For quantification of the relative positioning of the TES group within the feature space, the Euclidean distances between sham and TES groups and between the Dep and TES groups were measured, which showed that all TES group data points clustered closer to the sham group, whereas Dep group data points were clearly separated and located on the opposite side of the hyperplane (Figure 6J).

To assess the model performance beyond accuracy, we evaluated various statistical metrics derived from the results of the SVM. Specifically, F1 score, sensitivity, and specificity were evaluated to characterize class-wise discrimination under the one-versus-rest (OVR) framework, while the precision-recall area under the curve (PR-AUC) was used to assess ranking performance under moderate class imbalance. In addition, calibration was evaluated using the Brier score to quantify the reliability of predicted probabilities. Although the primary purpose of the pipeline was to investigate the separation effects of the TI-TES intervention on depression, such metrics were necessary to evaluate the stability of the resulting decision boundaries. The SVM pipeline involved classifying three groups (Dep, sham, and TES) through 5-fold cross-validation, so we examined performance at both the fold level (Figures S31 and S32) and the class level (Figure S33). Given the multiclass structure and the interest in class-specific separation, performance was evaluated under an OVR framework. Although the trained model showed high classification performance overall, occasional reductions in F1 score and sensitivity, accompanied by elevated Brier scores, were observed in specific folds. These patterns suggest fold-dependent variability in performance, which may reflect small-sample effects and sensitivity of the decision boundary to the composition of the training data rather than systematic model failure. Nonetheless, PR-AUC showed a consistent value of 1.00 under the OVR formulation, indicating perfect ranking of positive versus negative samples at the score level across folds. This result suggests that, despite variability in threshold-dependent metrics, the underlying score distributions for the classes remained well separated. This is in parallel with the purpose of the TI-TES treatment, which is to shift Dep individuals away from the depressive state and toward a sham-like profile. Class-wise performance assessment under the OVR framework further demonstrated that the Dep group was classified with high confidence across all folds, exhibiting minimal ambiguity and narrow variability across metrics. In contrast, the sham and TES groups showed lower mean performance values and larger error bars. This fold-dependent variability suggests partial overlap between sham and TES groups in feature space, reflecting their biological and behavioral proximity.

Having evaluated overall performance and stability, we next assessed whether the observed separation could be attributable to chance. To this end, a permutation test with 1,000 group-level label shuffles was performed (Figure S34). The observed cross-validated PR-AUC (1.00) exceeded all values obtained under permutation, yielding a significant empirical *p* value (one-sided permutation test, $p = 0.001$). This finding indicates that the observed separation is unlikely to be attributable to random label assignment. This conclusion was further supported by the aggregated confusion matrix, which showed high self-classification accuracy across all groups. In particular, the Dep group was classified without error, indicating a robust and stable separation from the other groups.

Next, standardized feature weights were analyzed to find directional patterns across cross-validation folds (Figure S35). Biological and neural feature groups showed positive weights for the TES class and negative weights for the sham and Dep classes, whereas behavioral features exhibited differences of largest magnitude, particularly in the depression group. Importantly, the sign of feature weights was highly stable across folds, suggesting that the computed decision boundaries were not driven by noise. Furthermore, bootstrap resampling (iteration $n = 2{,}000$) was conducted (Figure S36). For the TES class, biological, neural, and behavioral feature groups consistently exhibited positive coefficients, with 95% confidence intervals that did not overlap zero in most folds. In contrast, the depression

class showed consistently negative coefficients across feature groups, particularly for behavioral features, with larger magnitudes and narrower confidence intervals. Sham-related coefficients were clustered near zero but remained directionally consistent across folds, indicating a stable but weaker contribution to class separation. Importantly, the robust group discrimination achieved by the linear SVM cannot be attributed to any single strongly discriminative feature. Although several pairwise associations were observed at the univariate level, most did not remain significant after controlling group effects, indicating that these correlations were largely driven by between-group differences rather than intrinsic feature-feature relationships. Consistent with this observation, no individual variable exhibited a dominant effect capable of independently separating groups. Instead, classification performance appears to have emerged from the joint integration of multiple weak but complementary features spanning neural, behavioral, and biological domains. In such settings, multivariate classifiers can exploit coordinated patterns across features, including subtle covariation and partial redundancy, that are not detectable through univariate analyses alone. Thus, the observed separation in the linear feature space likely reflects distributed group-specific signatures encoded across multiple modalities rather than reliance on a single biomarker. While non-linear interactions cannot be entirely excluded in complex biological systems, the stability and interpretability of the linear decision boundary suggest that feature aggregation in a high-dimensional space was sufficient to capture the relevant group structure.

To assess model efficiency, we conducted a baseline classification using a logistic regression model trained on the identical dataset, with the same preprocessing and cross-validation protocol as the SVM in our framework (Figure S37). While sham and Dep were classified with accuracy similar to that of the SVM, TES showed a substantially lower classification accuracy of 30%. This discrepancy suggests that the linear decision boundaries learned by logistic regression were insufficient to capture the feature distributions associated with the TES class. This result indicates that the improved performance of the SVM is not attributable to trivial class separability but rather to its ability to construct more effective class margins under the same data and validation conditions.

Overall, we have classified the three groups with a trained SVM model pipeline and assessed its reliability. Linear scaling (depression score) and the SVM were conducted to validate the therapeutic effects of TI-TES, which together demonstrated that Dep and sham groups were clearly separable. The TES group consistently aligned with the sham group, supporting the therapeutic capacity of TI-TES.

DISCUSSION

While most smart contact lenses have been limited to monitoring metabolic or ocular diseases, this study introduces a wearable, non-invasive TI-TES contact lens as a bioelectronic strategy for depression treatment. By utilizing the retina as an accessible interface to the eye-brain axis, this platform circumvents the invasiveness and limited tolerability of conventional brain stimulation therapies. The contact lens integrates ultrathin Pt-decorated GaOx electrodes with selective Pt-nanocluster modification, achieving high transparency, mechanical compliance, and enhanced electrochemical performance. Through TI stimulation, localized low-frequency envelope fields are generated at the retina, and neural activations propagate along established eye-brain pathways, enabling targeted modulation of mood-related circuits while minimizing off-target ocular effects.

A key contribution of this work lies in its comprehensive multidisciplinary validation. Our behavioral analysis provided clear evidence of therapeutic efficacy. TI-TES-treated mice exhibited significant behavioral improvements in the OFT, indicating a reduction in anxiety and restoration of locomotor activity. Furthermore, immobility in the TST and FST was reduced significantly, demonstrating a reversal of depressive-like despair behaviors. In the three-chamber test, the TES group showed a remarkable improvement in social preference and novelty, restoring social interaction to levels comparable to those of the sham group. These behavioral findings were supported by electrophysiological and biological analyses, which revealed that the treatment restored disrupted neural connectivity, evidenced by a remarkable increase in phase locking and phase coherence in the theta band (HPC-PFC and HPC-HPC). To ensure the accuracy of these neural recordings and minimize tissue damage, we fabricated soft, biocompatible neural probes using liquid metals and a fluorinated elastomer. Our biological findings further confirmed that TI-TES treatment promoted neural recovery, as shown by a substantial recovery in total dendritic spine density, a significant increase in mature BDNF levels relative to the Dep group, and the mitigation of neuroinflammation. We utilized a machine-learning approach that provided an objective data-driven validation whereby the TI-TES-treated group was consistently aligned with the non-depressed control group across all behavioral, neural, and biological markers. These results underscore the therapeutic potential of using the retina as a precise interface for brain stimulation.

Our approach can be compared with light stimulation in terms of the mode of retinal activation. While both light-based and electrical stimulation engage retinal output pathways and propagate signals through overlapping eye-brain circuits, their mechanisms of activation differ. Photic stimulation activates retinal circuits through natural phototransduction in photoreceptors followed by synaptic relay to RGCs, providing physiologically natural retinal responses and being primarily optimized for visual and perceptual outcomes. However, its stimulation parameters are constrained by optical conditions, and repeated or prolonged use may induce visual percepts or visual fatigue, limiting its suitability for non-visual neuromodulation. In contrast, TI-TES directly depolarizes RGCs and inner retinal circuits through applied electric fields, enabling precise temporal control of neuronal firing independent of upstream phototransduction processes. Electrical stimulation is largely independent of external visual environments and reduces visual perceptual load, making it more suitable for repeated or prolonged neuromodulatory applications targeting non-visual brain circuits. These features make TI-TES advantageous for brain modulation via the retina-brain axis, particularly in psychiatric contexts. A summary comparison of the two stimulation modalities is provided in Table S1.

Recent studies have increasingly suggested that TES can influence brain function through the eye-brain axis, supported by well-established retinofugal pathways linking retinal output to thalamic, hypothalamic, and corticolimbic regions involved in mood and cognitive regulation.[71–73] Consistent with this framework, prior investigations have reported TES-associated modulation of neural oscillatory activity and functional connectivity as well as antidepressant-like behavioral and histological changes in preclinical models. For example, a previous study has reported that prolonged TES can induce long-lasting enhancements in functional and directional brain connectivity, including increased coherence and cross-frequency coupling between visual and prefrontal cortices, highlighting the capacity of retinal stimulation to modulate neural network dynamics relevant to higher-order brain functions.[74] Separately, other studies observed antidepressant-like behavioral effects of TES in rodent models accompanied by histological and molecular changes related to neuroplasticity, neurogenesis, and stress-related signaling pathways, supporting the biological plausibility of TES-mediated therapeutic effects.[75,76] Together, these prior studies establish an important foundation indicating that retinal electrical stimulation can influence both neural activity and behavior through the eye-brain axis. Building upon this body of work, the present study integrates these perspectives within a single experimental framework and further explores a refined stimulation paradigm based on TI-TES. By employing a temporally interferential electric field rather than conventional uniform stimulation, we were able to examine retina-brain neuromodulation while simultaneously evaluating behavioral, electrophysiological, and biological outcomes. In this regard, our findings complement existing TES literature and collectively support the concept that TES can serve as a viable route for modulating brain circuits relevant to psychiatric and neurodegenerative disorders.

In addition to demonstrating therapeutic efficacy, this study provides mechanistic evidence that TI-TES engages specific retinal-to-brain pathways to exert its antidepressant effects. Using *in vivo* epiretinal recordings, we showed that TI-TES evokes action-potential firing in RGCs, including ipRGCs, indicating direct activation of retinal output neurons. Importantly, VEP recordings further revealed that this retinal activation propagates to the visual cortex, as evidenced by a pronounced enhancement of the N1 component following TI-TES. Together, these electrophysiological findings establish that TI-TES engages functional RGC-mediated eye-brain circuits. To further determine whether these pathways are required for the therapeutic effects of TI-TES, we performed a pathway-disruption experiment using intravitreal NMDA injection to ablate RGCs. NMDA-induced RGC loss abolished the behavioral benefits of TI-TES in the OFT, demonstrating that intact RGC-dependent downstream pathways are necessary for the expression of TI-TES-induced antidepressant-like effects. This loss-of-function result, combined with the retinal and cortical electrophysiological evidence, provides causal support for the role of RGC- and ipRGC-associated pathways in mediating the therapeutic effects of TI-TES.

Despite the promising preclinical outcomes reported in this study, several practical challenges must be addressed to translate the TI-TES contact lens platform to human applications. First, the current study employed a wired configuration to ensure precise waveform control and stimulation stability during proof-of-concept validation. While suitable for controlled animal experiments, long-term human use will require full wireless integration encompassing power delivery, stimulation control, and real-time safety monitoring to ensure comfort, compliance, and robustness under natural eye movements and blinking. Second, inter-individual variability in ocular anatomy, tear film composition, corneal curvature, and tissue impedance may substantially influence stimulation efficiency and dosing, necessitating personalized calibration strategies and, potentially, closed-loop control schemes in clinical settings. Third, chronic and repeated use in humans introduces additional considerations related to long-term biocompatibility, ocular surface health, and inflammatory responses that cannot be fully captured in short-duration animal studies. Addressing these factors will be critical for ensuring safety and tolerability during extended wear.

The TI-TES strategy presented here, given the retina's deep anatomical and functional connections with the brain, has broad implications beyond depression. Future work will therefore focus on refining this platform toward a fully integrated, patient-friendly system, including wireless operation, personalized stimulation protocols, and long-term safety validation in large animal models, followed by rigorously designed human clinical trials. In addition, to further elucidate the broader neurophysiological impact of TI-TES, future studies will incorporate more comprehensive electrophysiological analyses, including power spectral characterization across the five frequency bands and comparisons across different subject groups. This will also include trials of TI-TES treatments on non-depressive individuals, which may help clarify both therapeutic and baseline neuromodulatory effects. Additionally, a more detailed exploration of the specific retinal cell types and pathways that are most responsive to TI-TES could inform the treatment of a wider spectrum of neurological and psychiatric conditions. Such large-scale, long-term studies represent the next major steps in advancing eye-based neurotherapies to clinical reality.

METHODS

Fabrication of TI-TES contact lens

The fabrication process of the TI-TES contact lens involves the following major steps.

(1) GaOx printing. To prepare the printing substrate, PDMS was first spin coated (4,000 rpm, 40 s) onto an SiO_2 wafer (Dasom RMS) as an adhesive layer, and a 25-μm-thick polyimide film was laminated. The printing procedure for GaOx was adapted from a previously reported study.[37] The liquid metal (EGaIn: 75.5% gallium, 24.5% indium alloy by weight; Changsha Santech Materials) was introduced into a custom-designed printer head, which was assembled by fixing two parallel glass slides with a 1-mm gap. After the printer head made initial contact with the substrate, it was retracted to a defined height of 300 μm to establish a stable meniscus. Printing was then carried out by translating the substrate on a motorized stage at a constant speed of 0.2 mm s^{-1}, while the printer head remained fixed.

(2) Pt-GaOx patterning. A sacrificial layer (LOR 3A photoresist, Kayaku) was photopatterned on printed GaOx layer followed by the deposition of Pt (1 nm) using e-beam evaporator on the TI-TES electrode. The sacrificial layer was subsequently removed through a lift-off development step (MR-REM 700, MicroChem), leaving Pt selectively on the designated TI-TES electrode regions. After Pt-GaOx patterning, a 1-μm-thick parylene layer was deposited via chemical vapor deposition for passivation. Openings for electrodes and pads were formed by patterning an additional photoresist layer (2,000 rpm, 40 s) and dry etching with oxygen plasma (reactive ion etching [RIE]; 100 W, 40 sccm O_2, 240 s).

(3) Deposition of Pt nanoclusters. A platinum electrodeposition solution was prepared by dissolving 0.25 g of platinum tetrachloride and 5 mg of lead acetate trihydrate (both from Sigma-Aldrich) in 25 mL of isopropyl alcohol at room temperature. The solution was ultrasonicated for 20 min and filtered to remove impurities. For electroplating, the TES electrode (cathode) and a Pt electrode (anode) were immersed in the solution and connected to a source meter (Keithley 2400, Tektronix). Electroplating was conducted by applying 2 V with a compliance current limit of 0.1 mA for a duration of 120 s.

(4) Lens molding. Prior to molding, a water-soluble polyethylene oxide (PEO) layer was coated onto the TI-TES electrode for protection during lens fabrication. The TI-TES electrode was then placed into a contact lens mold, which was filled with a silicone elastomer precursor (Interojo). The filled mold was cured at 70°C for 5 h under a pressure of 313 kPa. After curing, the lens material covering the TI-TES electrode was carefully removed, and the device was immersed in deionized water at 60°C for 2 h to fully dissolve the PEO layer.

Electrical characterization of electrodes

Impedance characterization of the TI-TES electrodes was carried out in phosphate-buffered saline (PBS, Sigma-Aldrich). A multichannel potentiostat (PMC-1000, AMETEK) was used to record impedance data across a frequency range spanning from 0.01 kHz to 100 kHz.

Cyclic voltammetry measurements were performed in PBS using a PMC-1000 multichannel potentiostat (AMETEK). The potential was swept from −0.6 V to 0.8 V versus Ag/AgCl reference electrode at a scan rate of 50 mV s^{-1}.

For voltage transients, after immersing the TI-TES electrodes in PBS, current-controlled biphasic pulses with cathodic amplitudes ranging from 0.4 to 1.6 mA in 0.4-mA increments were applied (pulse width 200 μs, interpulse interval 40 μs). Electrode was monitored by recording voltage waveforms against an Ag/AgCl reference electrode, using a multichannel potentiostat (PMC-1000, AMETEK). The CIC was extracted from these voltage transients by determining the maximum charge delivered before reaching the water window potential (−0.6 V).

Biocompatibility and cytotoxicity assessment

The human corneal epithelial cell line HCE-2 (ATCC, CRL-11135, clone 50.B1) was maintained in a mixed culture medium consisting of DMEM/F-12 and RPMI-1640 (Gibco, MD, USA), supplemented with 10% heat-inactivated fetal bovine serum (FBS), 50 U mL^{-1} penicillin, and 50 μg mL^{-1} streptomycin. Cells were seeded at a concentration of 1×10^5 cells ml^{-1} in 96-well plates. Prior to testing, the TI-TES lenses were sterilized by immersion in 70% ethanol for 3 min, followed by three rinses in PBS, each lasting 2 min. To prepare the extraction medium, TI-TES lenses (TES group) and commercial soft contact lenses (control group) were incubated separately in culture medium containing 2% FBS at 37°C for 24 h. The resulting soaking solutions—referred to as soaking-induced medium (SIM)—were collected and stored at −80°C until analysis. For testing, 100 μL of either SIM was added to each well and incubated with the cells for 24 h. Cell viability was assessed using a combination of fluorescence imaging and metabolic assay. Live cells were stained with calcein (excitation/emission ~495/515 nm) and dead cells with SYTOX Deep Red (excitation/emission maxima ~660/628 nm) according to the manufacturer's protocol (Invitrogen, MA, USA). Following staining and several PBS washes, images were captured using a fluorescence microscope (BX51; Olympus, Tokyo, Japan).

In parallel, a colorimetric viability assay was performed using Cell Counting Kit-8 (CCK-8, Dojindo). After 24-h exposure to the test extracts, 10 μL of CCK-8 reagent was added to each well, followed by a 2-h incubation at 37°C in a 5% CO_2 atmosphere. Absorbance was measured at 450 nm using a microplate reader (VersaMax, Molecular Devices), and cell viability was calculated based on the optical density values.

Animal experiments

All experimental protocols were approved by the Yonsei University Institutional Animal Care and Use Committee (IACUC-202307-1709-03 and IACUC-202501-1997-01) and followed the institutional guidelines outlined in the Guide for the Care and Use of Laboratory Animals. Male C3H/HeNCrlOri (rd1) mice (8 weeks old) and male C57BL/6 mice (8 weeks old) were individually housed in stainless-steel cages (26 × 20 × 13 cm) under controlled environmental conditions: 24°C room temperature, 55% relative humidity, and a 12/12-h light/dark cycle. Because TI-TES engages vision-related neural pathways, rd1 mice—characterized by photoreceptor degeneration—were used to eliminate visual input as a confounding variable in neural pathway activation. Accordingly, all experiments related to depression evaluation and therapeutic efficacy, including behavioral tests, neural electrophysiology, and brain histological analyses, were conducted exclusively in rd1 mice. In contrast, C57BL/6 mice were used solely for ocular safety and biocompatibility assessments, including corneal and retinal H&E staining and evaluation of tissue integrity following TI-TES application, as their intact ocular structures allow reliable histological assessment. No behavioral, neural, or depression-related analyses were performed in C57BL/6 mice.

Corticosterone treatment

A chronic corticosterone-induced stress mouse model recapitulating depression-associated behavioral phenotypes was established following the protocol outlined by Pereira et al.[77] C3H/HeNCrlOri (rd1, 25–30 g, male) mice were randomized into three

groups, including the control (sham group), depression (Dep group), and TI-TES treatment (TES group). For depression induction, corticosterone by subcutaneous administration (s.c.) of a total 100 μL of corticosterone cocktail (20 mg kg^{-1} body weight) dissolved in 20% Tween 80, 0.2% DMSO (all purchased from Sigma, St. Louis, MO), and 0.9% saline were chronically treated. It should be noted that the corticosterone paradigm used in this study does not represent human major depressive disorder itself but rather a preclinical stress model that recapitulates specific behavioral and biological features associated with depression. Therefore, the therapeutic effects demonstrated here should be interpreted as modulation of depression-like phenotypes rather than direct treatment of the human disorder.

Different administration periods were applied for the Dep and TES groups. The Dep group received corticosterone for 3 weeks, whereas the TES group received corticosterone for 6 weeks. This difference was intentional and reflected the experimental design, in which TI-TES treatment was initiated after induction of depressive behaviors while corticosterone administration was maintained during the intervention period. The rationale for this design is described in detail in Note S2.

Fluoxetine treatment

Following the establishment of the depression model by chronic corticosterone administration, a subset of depressed mice was subjected to fluoxetine treatment as a pharmacological reference group. After 3 weeks of corticosterone treatment at the full dose (20 mg kg^{-1}, s.c.), fluoxetine hydrochloride (Sigma) was administered by daily subcutaneous injection for an additional 3 consecutive weeks. Fluoxetine hydrochloride was prepared based on a previously established protocol by dissolving the compound in a vehicle containing DMSO, NaCl, and distilled water to achieve a final dose of 20 mg kg^{-1}, with the injection volume adjusted according to body weight (192–208 μL for mice weighing 24–26 g). During the fluoxetine treatment period, corticosterone administration was continued to prevent spontaneous recovery from depressive-like behaviors, thereby maintaining a stable depression state throughout the treatment phase.

Soft neural probe fabrication

The soft neural probe was fabricated through the following sequence of steps. (1) A silicon wafer (Dasom RMS, Republic of Korea) was first coated with an LOR 3A lift-off resist (MicroChem) by spin coating, serving as a sacrificial layer. (2) For the bottom soft layer, fluorinated soft negative photoresist (Fleuron PR-USF, Axoft) was spin coated on the wafer (1,000 rpm) to obtain a thickness of 2.5 μm. (3) A spin-coated bottom layer was patterned by UV light with a nitrogen diffuser. The exposed layer was then baked at 115°C and developed in developer (DEV-10, Axoft). (4) For surface treatment, oxygen plasma at 100 W for 60 s under an O_2 flow of 40 sccm was treated using RIE. (5) EGaIn was printed to 4-μm-wide lines on this bottom layer. (6) An additional 2.5-μm-thick layer of fluorinated soft negative photoresist was spin coated to serve as the top encapsulation layer of the neural probe. (6) The fluorinated soft negative photoresist layer was photolithographically patterned so that the electrode tip regions were exposed. (7) Pt nanocluster was deposited on exposed the EGaIn tip region by electroplating as mentioned above (applying 2 V with a compliance current limit of 0.1 mA for a duration of 120 s).

Neural probe implantation and electrophysiological recording

Neural probes were implanted into specific stereotaxic coordinates of HPC and PFC of mouse brain. One electrode was implanted into the PFC (anteroposterior [AP] +1.7 mm, mediolateral [ML] +0.7 mm, dorsoventral [DV] −2.5 mm), and two electrodes were implanted into the HPC (AP −2.0 mm, ML ±2.0 mm, DV −2.0 mm), one on each side about the bregma, of which one is used as the working electrode and the other as the reference electrode. An electrophysiological recording system was used for the recording of LFPs and SUs. The system is composed of an RZ2 amplifier processor, PZ5 neurodigitizer, MZ60 MEA interface (Tucker-Davis Technologies, USA), and Synapse software on a computer. Different band-pass filters were used for LFP and SU recording. For LFPs, a 0.1- to 300-Hz band-pass filter was used, and for SUs a 300- to 3,000-Hz band-pass filter was used.

H&E staining of mouse cornea and retina

H&E staining was performed on mouse ocular tissue to evaluate histological changes before and after TI-TES treatment. H&E staining was conducted using C57BL/6 mice instead of rd1 mice, as rd1 mice already exhibit retinal tissue damage, which would hinder accurate evaluation of TI-TES-induced changes in both the cornea and retina. The eyeballs were initially fixed in 4% paraformaldehyde, followed by paraffin embedding. Serial sections with a thickness of 5 μm were obtained using a microtome. For nuclear staining, the sections were incubated in Harris' hematoxylin at 60°C–70°C for 6 h and then rinsed thoroughly with deionized water. To differentiate the stained nuclei, tissues were treated sequentially with 10% acetic acid for 2 h and 85% ethanol for 10 h, followed by rinsing in running tap water. Bluing was achieved by immersing the sections in a saturated lithium carbonate solution for 12 h. After another rinse with tap water, cytoplasmic staining was performed using eosin Y dissolved in ethanol, with an incubation period of 48 h.

NMDA-induced RGC degeneration model

To induce excitotoxic RGC degeneration, NMDA (Sigma-Aldrich, M3262) was administered via intravitreal injection as previously described, with minor modifications. In brief, mice were anesthetized by intraperitoneal injection of a Zoletil/Rompun cocktail, and pupils were dilated using topical tropicamide. NMDA was dissolved in sterile PBS at a concentration of 20 mM, and 2 μL of the solution was intravitreally injected into the right eye using a Hamilton syringe fitted with a 33-gauge needle. The contralateral eye received an equal volume of PBS as a vehicle control. Care was taken to avoid lens injury during the injection procedure. Seven days after injection, mice were euthanized and eyes were enucleated for histological analysis. Retinal sections were subjected to H&E staining. Cell loss in the GCL was assessed by counting the number of nuclei within the GCL per high-power field (HPF) in a masked manner. HPFs were acquired using a 40× objective, and values from multiple representative fields were averaged for each biological replicate. GCL cell

counts were used as a surrogate measure of NMDA-induced RGC degeneration.

Corneal and retinal immunofluorescence staining

For immunofluorescence analysis, paraffin sections were deparaffinized and rehydrated, followed by heat-induced antigen retrieval using citrate buffer (pH 6.0) in a microwave oven. Sections were permeabilized with 0.1%–0.3% Triton X-100 in PBS and blocked for 1 h at room temperature with blocking buffer containing 5% bovine serum albumin and 2% normal donkey serum. Primary antibodies against CD45 (Invitrogen, 14-0451-82) or Iba1 (Abcam, ab178846) were applied overnight at 4°C. After washing, donkey-derived fluorescent secondary antibodies were incubated at room temperature, and nuclei were counterstained with DAPI. Images were acquired using a fluorescence microscope under identical exposure settings for all experimental groups.

For the TUNEL assay, apoptotic cells were detected using a commercially available TUNEL assay kit according to the manufacturer's instructions. TUNEL-positive cells were quantified per HPF within anatomically defined corneal or retinal tissue regions, as identified by DAPI staining. Fluorescence signals detected outside tissue boundaries were excluded from analysis. HPFs were acquired using a 40× objective, and values from multiple fields were averaged for each biological replicate.

Mouse brain immunohistochemistry and Golgi-Cox staining

Mouse brains were removed and fixed in 4% paraformaldehyde (Biosesang, Seoul, Korea) overnight at 4°C and washed with PBS three times. Tissues were embedded in paraffin and sectioned at a thickness of 5 μm using a Leica HisoCore Nanocut microtome. Sections were stained with an H&E stain kit according to the protocol provided by Vector Laboratories (CA, USA), and images were obtained under a microscope (Olympus BX53M, Tokyo, Japan). For immunohistochemical staining, sections were immersed in 100% MeOH for 5 min, followed by incubation in 10 mM citrate (Sigma-Aldrich, pH 6.0) for 10 min at a temperature higher than 90°C. After three washes in PBS, tissue was blocked with 5% horse serum for 1 h and then incubated overnight at 4°C with anti-NeuN-AF555 (Merck, cat. #53-9892-82) and anti-GFAP-AF488 (Thermo Fisher, cat. #MAB377A5) conjugated antibodies (1:300). Nuclei were visualized using a fluorescence microscope with an antifade mounting medium containing DAPI (Vector Laboratories). Fluorescence images were captured using an Axio Observer Z1 LSM780 confocal microscope (Carl Zeiss, Oberkochen, Germany). The densities of GFAP-positive and NeuN-positive cells were analyzed using ImageJ.

Golgi-Cox staining of the mouse brain was performed using an FD Rapid GolgiStain Kit according to the protocol provided by FD NeuroTechnologies (Columbia, MD, USA). The Golgi-Cox kit is based on the principle of the methods described by Ramón-Moliner[78] and Glaser and Van der Loos.[79] Fresh, non-perfused brain from each group was used and immersed in various solutions. The brain was coronally sectioned at a thickness of 100 μm using a cryomicrotome (model CM3050 S, Leica, Germany) and dried for 48 h at room temperature in the dark room. After staining, the slice was cleaned and mounted with Eukitt Quick-hardening mounting medium. Images were captured using an Olympus microscope equipped with a 100× objective lens (Olympus BX53M, Tokyo, Japan).

RT-qPCR

Total RNA was purified using TRIzol reagent (Invitrogen, cat. #15596-026), and 1 μg μL^{-1} of total RNA was reverse transcribed in a thermal cycler using a Revert First Strand cDNA Synthesis Kit (Fenmentas-Thermo, cat. #K1622) following the manufacturer's protocol (Thermo Fisher). RT-qPCR for IL-6 and TNF-α was performed using specific primers and SYBR Green master mix (2× Roche, 04707516001) on a LightCycler 480 Instrument II (Roche) according to the user manual. The cycling conditions were as follows: 50°C for 2 min, 95°C for 10 min, followed by 40 cycles of 15 s at 95°C and 1 min at 60°C, and a final step of 15 s at 95°C. The primers sequences used for amplification were as follows: IL-6 (GenBank: NM_031168.1) forward, 5′-TACCACTTCACAAGTCGGAGGC-3′ and reverse, 5′-GAACAACGATGATGCACTTGCAG-3′; TNF-α (GenBank: NM_013693.3) forward, 5′-GGTGCCTATGTCTCAGCCTCTT-3′ and reverse, 5′-CTCCC TCTCATCAGTTCTATGGC-3′; GAPDH (GenBank: NM_002046.7) forward, 5′-GTCTTCACCACCATGGAGAAGG-3′ and reverse, 5′- CTGGCCAAGGTCATCCATGA-3′ (Cosmo Genetech, Seoul, Korea). RT-qPCR reactions were performed using 1 μL of cDNA per reaction. To control potential effects of TES on cytokine expression levels, the housekeeping gene glyceraldehyde-3-phosphate dehydrogenase (GAPDH) was used as an endogenous control.

ELISA

Blood samples were collected from the cardiac puncture into EDTA tubes (BD, Vacutainer K2 EDTA 5.4 mg, cat, #367856) and allowed to stand for 30 min at room temperature. They were then centrifuged at 3,000 rpm for 15 min, and the supernatant was collected and stored at −80°C until analysis. The corticosterone (mouse Corticosterone ELISA Kit, Elabscience, cat. #E-EL-0161) and serotonin (mouse Serotonin ELISA Kit, Elabscience, cat. #E-EL-0033) levels were measured in duplicate using the ELISA kit according to the manufacturer's recommended protocol.

The brain tissue was homogenized in RIPA buffer (Thermo Fisher, cat. #89900) and centrifuged at 12,000 rpm for 30 min. The supernatant was collected and stored at −80°C until analysis. BDNF levels were quantified in duplicate using the mouse mature BDNF Rapid ELISA Kit (Biosensis, cat. #BEK-2211-1P) following the manufacturer's instructions. Absorbance was measured at 450 nm using a microplate reader to determine the BDNF concentration in the sample.

Power spectrum measurement

The same pipeline was applied to two pieces of signal recording (before and after TI-TES treatment), both with a duration of 10 s. The time-frequency and band-specific features were extracted from the raw time-domain signals using a short-time Fourier transform (STFT)-based analysis. The raw signal was firstly transformed into the time-frequency domain via STFT, yielding a spectrogram along with corresponding frequency and time

axes. Both the original STFT and a normalized version of the STFT were computed using identical analysis parameters. The normalized spectrogram was used to facilitate relative comparisons of spectral dynamics across time, while the original spectrogram was retained to examine absolute power distributions. To reduce local fluctuations and enhance the stability of spectral estimates, a 2D averaging filter of size 2×16 was applied to the STFT matrices. This smoothing operation was performed across both the frequency and time dimensions, thereby attenuating transient noise and emphasizing broader spectral patterns at the band level. Using the normalized spectrogram, band-specific power measures were calculated for predefined frequency ranges (delta, 0.5–4 Hz; theta, 4–8 Hz; alpha, 8–12 Hz; beta, 12–28 Hz; gamma, 28–100 Hz). For each frequency band, the spectral values within the corresponding frequency bins were averaged across the frequency dimension at each time point, resulting in a time-resolved band power signal. In addition, the mean of each band power time series was computed over the entire recording period to obtain a single representative power value per band. Furthermore, additional time-based features were derived using a sliding window approach with a window length of 0.5 s. For each window, band-limited signal components were extracted, and the mean square value of the band amplitude was calculated, providing an estimate of band-specific power within that time segment. In parallel, the filtered signal within the same window was transformed using fast Fourier transform, and the sum of the magnitudes of the resulting spectrum was computed as a measure of the overall spectral content. These features collectively quantified temporal variations in band-specific energy and frequency-domain characteristic of the signal.

Phase-locking analysis

Spike-LFP phase-locking analysis was conducted using a time-aligned and frequency-resolved computational procedure. For each detected spike, a temporal window spanning 0.5 ms before and 1.0 ms after the spike peak was defined. The window length was converted from milliseconds to sample indices based on the temporal resolution of the recording. Spike peak timestamps were used to extract time-aligned signal segments and identify the corresponding LFP sample indices. The LFP signal was band-pass filtered within a predefined frequency range, and the instantaneous phase of the filtered signal was computed. For each spike, the LFP phase at the spike peak time was extracted, resulting in a vector of phase values associated with spike occurrences. Phase values were converted to unit vector using sine and cosine transformations, and the mean resultant vector was computed by averaging across spikes. The magnitude of this vector was used as the PLV, and its angle represented the mean phase of spike locking. Statistical significance of phase locking was evaluated using the Rayleigh test applied to the circular phase distribution. To assess frequency-dependent phase locking, the same computational steps were repeated across multiple frequency bands by sequentially band-pass filtering the LFP signal in predefined ranges. Phase values, PLVs, and Rayleigh test p values were computed independently for each frequency band. For visualization, phase angles were discretized into bins spanning 0°–360°, and for each bin the number of frequencies showing phase locking at the corresponding phase was counted. The binned phase-frequency counts were visualized using rose plots.

Phase-coherence analysis

Phase coherence between the two LFP signals was quantified based on the distribution of instantaneous phase differences. The raw LFP signals were first band-pass filtered within predefined frequency ranges, identical to these used for the power spectrum (delta, 0.5–4 Hz; theta, 4–8 Hz; alpha, 8–12 Hz; beta, 12–28 Hz; gamma, 28–100 Hz). For a given frequency band, the instantaneous phase of each filtered signal was computed at every time point. Phase differences were calculated by subtracting the instantaneous phase of one signal from the other at corresponding time points. Negative phase differences were adjusted by adding 360° to constrain all values to the range of 0°–360°. Each phase difference was then converted into a unit vector using cosine and sine transformations. The mean resultant vector was obtained by averaging these unit vectors across all time points. Phase coherence was defined as the magnitude of the mean resultant vector, yielding a value between 0 and 1. The mean phase difference was calculated from the angle of the mean resultant vector, with quadrant correction applied to ensure proper representation within the 360° range. Frequency-resolved phase coherence was computed using the same procedure across narrow frequency bands. The LFP signals were sequentially band-pass filtered in 1-Hz-wide frequency ranges from 0.5 to 100 Hz. For each frequency band, instantaneous phases were extracted, phase differences were computed and normalized to 0°–360°, and phase coherence was calculated as the magnitude of the mean resultant vector. This process yielded a phase coherence spectrum representing coherence values as a function of frequency. For band-averaged analysis, phase coherence was computed once per predefined frequency band by pooling phase differences across the entire band, resulting in a single coherence value for each band.

Data preprocessing in machine learning

(1) Missing data: no data were missing across the biological, behavioral, and neural analyses, so no missing data-handling procedures were performed.
(2) Correlation analysis (chord diagram): a correlation analysis was conducted to identify the relationships between the factors. A customized Python script was used to calculate the Pearson correlation coefficients between the factors. All coefficients were converted to absolute values to focus on the magnitude of the associations. The calculated magnitudes of the correlation coefficients were visualized as the thickness of the chords in the chord diagram.
(3) Feature selection (Sankey diagram): to identify and eliminate features with minimal association to the depression score, a feature evaluation was conducted using a customized Python script. Pearson correlation coefficients between the factors and the depression score were computed and visualized using a Sankey diagram, where the magnitudes of the coefficients were represented by the thickness of the links.

(4) Data normalization (min-max scaling): for every factor, the acquired data for all animals were aligned from the minimum to maximum.

Classification in machine learning

Two machine-learning methods were used to assess the therapeutic effects of TI-TES. Both methods were performed using customized Python codes.

(1) In the first method, t-SNE, which is an unsupervised learning approach, data were applied to the codes without labels to inform whether the data are from a sham, TES, or depression group. A t-SNE module from the Python database was implemented to calculate the relative distances between the data points in its original multidimensional axes. The calculated relative distances were used to project the points in a 2D space.
(2) In the second method, the SVM, the data were first scatterplotted in a 3D space, with the axes headings of biological data, neural data, and behavioral data. A hyperplane that divided the sham and depression data points was then computed using the SVM library embedded in the Python database.

Statistical analysis

All data are presented as mean ± standard deviation (SD). Statistical analyses were performed using open-source MATLAB code (R2021a). For comparisons, one-way analysis of variance (ANOVA) was first applied to assess overall group differences. When a significant main effect was detected, post hoc pairwise comparisons were performed using unpaired one-sided Student's *t* tests with Holm-Bonferroni correction to control for multiple testing.

RESOURCE AVAILABILITY

Lead contact

Further information and requests for resources and reagents should be directed to and will be fulfilled by the lead contact, Jang-Ung Park (jangung@yonsei.ac.kr).

Materials availability

This study did not generate new, unique reagents.

Data and code availability

- All data reported have been deposited at the Zenodo repository and are publicly available as of the date of publication under https://doi.org/10.5281/zenodo.19236828.
- This paper does not report original code.
- Any additional information required to reanalyze the data reported in this paper is available from the lead contact upon request.

ACKNOWLEDGMENTS

This work was supported by the Ministry of Science & ICT (MSIT), the Ministry of Trade, Industry and Energy, the Ministry of Health & Welfare, and the Ministry of Food and Drug Safety of Korea through the National Research Foundation (RS-2023-NR077138, RS-2024-00464032, RS-2025-16063568, and RS-2025-18362970), STEAM Research Programs (RS-2024-00460364), ERC Program (RS-2024-00406240), Technology Innovation Program (RS-2025-08672969), and Korea Institute of Science and Technology Institutional Program (2E33191 and 2E33190). The authors acknowledge the financial support by the Institute for Basic Science (IBS-R026-D1). This work was also supported from the Yonsei University Research Fund (Post Doc. Researcher Supporting Program) of 2025 (2025-12-0195).

AUTHOR CONTRIBUTIONS

W.P. and J.P. contributed to ideation and conducted the literature research; W.P. and J.P. participated in the comprehensive planning of the experiment, fabrication of the TI-TES lens, conducting animal experiments, machine-learning-based analysis, and overall manuscript composition; Y.-M.H. and H.S. were responsible for conducting all animal experiments and molecular analysis; Enji Kim and J.L. conducted neural signal recording and analysis; W.G.C. and S.H.A. contributed to the optimization of TI-TES fabrication process and conducted the evaluation and analysis of the electrical properties of the TI-TES electrodes; Eunmin Kim and I.J. contributed to the optimization of neural probe fabrication process; M.S.C. and S.H.B. performed ocular tissue safety and biocompatibility assessments, including histological and fluorescence imaging analyses; S.K. contributed to the analysis of behavioral experiments; and J.-U.P. oversaw all of the research phases and revised the manuscript. All authors participated in writing and reviewing the manuscript.

DECLARATION OF INTERESTS

The authors declare no competing interests.

SUPPLEMENTAL INFORMATION

Supplemental information can be found online at https://doi.org/10.1016/j.xcrp.2026.103303.

Received: October 7, 2025
Revised: February 19, 2026
Accepted: April 13, 2026
Published: May 14, 2026, corrected online July 2, 2026

REFERENCES

1. Shin, J., Song, J.W., Flavin, M.T., Cho, S., Li, S., Tan, A., Pyun, K.R., Huang, A.G., Wang, H., Jeong, S., et al. (2025). A non-contact wearable device for monitoring epidermal molecular flux. Nature *640*, 375–383. https://doi.org/10.1038/s41586-025-08825-2.
2. Chang, A.-Y., Lin, M., Yin, L., Reynoso, M., Ding, S., Liu, R., Dugas, Y., Casanova, A., Park, G., Li, Z., et al. (2026). Integration of chemical and physical inputs for monitoring metabolites and cardiac signals in diabetes. Nat. Biomed. Eng. *10*, 94–109. https://doi.org/10.1038/s41551-025-01439-z.
3. Heng, W., Yin, S., Min, J., Wang, C., Han, H., Shirzaei Sani, E., Li, J., Song, Y., Rossiter, H.B., and Gao, W. (2024). A smart mask for exhaled breath condensate harvesting and analysis. Science *385*, 954–961. https://doi.org/10.1126/science.adn6471.
4. Nyein, H.Y.Y., Bariya, M., Tran, B., Ahn, C.H., Brown, B.J., Ji, W., Davis, N., and Javey, A. (2021). A wearable patch for continuous analysis of thermoregulatory sweat at rest. Nat. Commun. *12*, 1823. https://doi.org/10.1038/s41467-021-22109-z.
5. Choi, S., Han, S.I., Jung, D., Hwang, H.J., Lim, C., Bae, S., Park, O.K., Tschabrunn, C.M., Lee, M., Bae, S.Y., et al. (2018). Highly conductive, stretchable and biocompatible Ag–Au core–sheath nanowire composite for wearable and implantable bioelectronics. Nat. Nanotechnol. *13*, 1048–1056. https://doi.org/10.1038/s41565-018-0226-8.
6. Li, P., Zhang, J., Hayashi, H., Yue, J., Li, W., Yang, C., Sun, C., Shi, J., Huberman-Shlaes, J., Hibino, N., and Tian, B. (2024). Monolithic silicon for high spatiotemporal translational photostimulation. Nature *626*, 990–998. https://doi.org/10.1038/s41586-024-07016-9.
7. Sheng, H., Liu, R., Li, Q., Lin, Z., He, Y., Blum, T.S., Zhao, H., Tang, X., Wang, W., Jin, L., et al. (2025). Brain implantation of soft bioelectronics

via embryonic development. Nature *642*, 954–964. https://doi.org/10.1038/s41586-025-09106-8.

8. Li, H., Tan, P., Rao, Y., Bhattacharya, S., Wang, Z., Kim, S., Gangopadhyay, S., Shi, H., Jankovic, M., Huh, H., et al. (2024). E-Tattoos: Toward Functional but Imperceptible Interfacing with Human Skin. Chem. Rev. *124*, 3220–3283. https://doi.org/10.1021/acs.chemrev.3c00626.
9. Kim, M.S., Kim, M.S., Lee, M., Jang, H.J., Kim, D.H., Chang, S., Kim, M., Cho, H., Kang, J., Choi, C., et al. (2024). Feline eye–inspired artificial vision for enhanced camouflage breaking under diverse light conditions. Sci. Adv. *10*, eadp2809. https://doi.org/10.1126/sciadv.adp2809.
10. Sim, K., Ershad, F., Zhang, Y., Yang, P., Shim, H., Rao, Z., Lu, Y., Thukral, A., Elgalad, A., Xi, Y., et al. (2020). An epicardial bioelectronic patch made from soft rubbery materials and capable of spatiotemporal mapping of electrophysiological activity. Nat. Electron. *3*, 775–784. https://doi.org/10.1038/s41928-020-00493-6.
11. Lee, W.W., Tan, Y.J., Yao, H., Li, S., See, H.H., Hon, M., Ng, K.A., Xiong, B., Ho, J.S., and Tee, B.C.K. (2019). A neuro-inspired artificial peripheral nervous system for scalable electronic skins. Sci. Robot. *4*, eaax2198. https://doi.org/10.1126/scirobotics.aax2198.
12. Xu, Y., De la Paz, E., Paul, A., Mahato, K., Sempionatto, J.R., Tostado, N., Lee, M., Hota, G., Lin, M., Uppal, A., et al. (2023). In-ear integrated sensor array for the continuous monitoring of brain activity and of lactate in sweat. Nat. Biomed. Eng. *7*, 1307–1320. https://doi.org/10.1038/s41551-023-01095-1.
13. Yin, S., Yao, D.R., Song, Y., Heng, W., Ma, X., Han, H., and Gao, W. (2024). Wearable and Implantable Soft Robots. Chem. Rev. *124*, 11585–11636. https://doi.org/10.1021/acs.chemrev.4c00513.
14. Vasconcelos, L.S. de, Yan, Y., Maharjan, P., Kumar, S., Zhang, M., Yao, B., Li, H., Duan, S., Li, E., Williams, E., et al. (2025). On-scalp printing of personalized electroencephalography e-tattoos. Cell Biomater. *1*, 100004. https://doi.org/10.1016/j.celbio.2024.100004.
15. Krishnan, V., and Nestler, E.J. (2008). The molecular neurobiology of depression. Nature *455*, 894–902. https://doi.org/10.1038/nature07455.
16. Insel, T.R., and Cuthbert, B.N. (2015). Brain disorders? Precisely. Science *348*, 499–500. https://doi.org/10.1126/science.aab2358.
17. Bremner, J.D., Narayan, M., Anderson, E.R., Staib, L.H., Miller, H.L., and Charney, D.S. (2000). Hippocampal Volume Reduction in Major Depression. Am. J. Psychiatry *157*, 115–118. https://doi.org/10.1176/ajp.157.1.115.
18. Drysdale, A.T., Grosenick, L., Downar, J., Dunlop, K., Mansouri, F., Meng, Y., Fetcho, R.N., Zebley, B., Oathes, D.J., Etkin, A., et al. (2017). Resting-state connectivity biomarkers define neurophysiological subtypes of depression. Nat. Med. *23*, 28–38. https://doi.org/10.1038/nm.4246.
19. Martinowich, K., Manji, H., and Lu, B. (2007). New insights into BDNF function in depression and anxiety. Nat. Neurosci. *10*, 1089–1093. https://doi.org/10.1038/nn1971.
20. Duman, R.S., Aghajanian, G.K., Sanacora, G., and Krystal, J.H. (2016). Synaptic plasticity and depression: new insights from stress and rapid-acting antidepressants. Nat. Med. *22*, 238–249. https://doi.org/10.1038/nm.4050.
21. Berton, O., and Nestler, E.J. (2006). New approaches to antidepressant drug discovery: beyond monoamines. Nat. Rev. Neurosci. *7*, 137–151. https://doi.org/10.1038/nrn1846.
22. Semkovska, M., and McLoughlin, D.M. (2010). Objective Cognitive Performance Associated with Electroconvulsive Therapy for Depression: A Systematic Review and Meta-Analysis. Biol. Psychiatry *68*, 568–577. https://doi.org/10.1016/j.biopsych.2010.06.009.
23. Mayberg, H.S., Lozano, A.M., Voon, V., McNeely, H.E., Seminowicz, D., Hamani, C., Schwalb, J.M., and Kennedy, S.H. (2005). Deep Brain Stimulation for Treatment-Resistant Depression. Neuron *45*, 651–660. https://doi.org/10.1016/j.neuron.2005.02.014.
24. Jacobson, M., and Hirose, G. (1978). Origin of the Retina from Both Sides of the Embryonic Brain: A Contribution to the Problem of Crossing at the Optic Chiasma. Science *202*, 637–639. https://doi.org/10.1126/science.705349.
25. LeGates, T.A., Fernandez, D.C., and Hattar, S. (2014). Light as a central modulator of circadian rhythms, sleep and affect. Nat. Rev. Neurosci. *15*, 443–454. https://doi.org/10.1038/nrn3743.
26. Mahoney, H.L., and Schmidt, T.M. (2024). The cognitive impact of light: illuminating ipRGC circuit mechanisms. Nat. Rev. Neurosci. *25*, 159–175. https://doi.org/10.1038/s41583-023-00788-5.
27. Wu, F., Lu, Q., Kong, Y., and Zhang, Z. (2023). A Comprehensive Overview of the Role of Visual Cortex Malfunction in Depressive Disorders: Opportunities and Challenges. Neurosci. Bull. *39*, 1426–1438. https://doi.org/10.1007/s12264-023-01052-7.
28. Zhang, X., Bullard, K.M., Cotch, M.F., Wilson, M.R., Rovner, B.W., McGwin, G., Owsley, C., Barker, L., Crews, J.E., and Saaddine, J.B. (2013). Association Between Depression and Functional Vision Loss in Persons 20 Years of Age or Older in the United States, NHANES 2005-2008. JAMA Ophthalmol. *131*, 573–581. https://doi.org/10.1001/jamaophthalmol.2013.2597.
29. Sehic, A., Guo, S., Cho, K.-S., Corraya, R.M., Chen, D.F., and Utheim, T.P. (2016). Electrical Stimulation as a Means for Improving Vision. Am. J. Pathol. *186*, 2783–2797. https://doi.org/10.1016/j.ajpath.2016.07.017.
30. Zhou, W., Huang, Z., Xu, K., Li, Y., Li, X., Li, J., Jin, Y., Snellingen, T., and Liang, L. (2024). Transpalpebral electrical stimulation for the treatment of retinitis pigmentosa: study protocol for a series of N-of-1 single-blind, randomized controlled trial. Trials *25*, 89. https://doi.org/10.1186/s13063-024-07933-0.
31. Mirzakhalili, E., Barra, B., Capogrosso, M., and Lempka, S.F. (2020). Biophysics of Temporal Interference Stimulation. Cell Syst. *11*, 557–572.e5. https://doi.org/10.1016/j.cels.2020.10.004.
32. Grossman, N., Bono, D., Dedic, N., Kodandaramaiah, S.B., Rudenko, A., Suk, H.-J., Cassara, A.M., Neufeld, E., Kuster, N., Tsai, L.-H., et al. (2017). Noninvasive Deep Brain Stimulation via Temporally Interfering Electric Fields. Cell *169*, 1029–1041.e16. https://doi.org/10.1016/j.cell.2017.05.024.
33. Violante, I.R., Alania, K., Cassarà, A.M., Neufeld, E., Acerbo, E., Carron, R., Williamson, A., Kurtin, D.L., Rhodes, E., Hampshire, A., et al. (2023). Non-invasive temporal interference electrical stimulation of the human hippocampus. Nat. Neurosci. *26*, 1994–2004. https://doi.org/10.1038/s41593-023-01456-8.
34. Hutcheon, B., Yarom, Y., Hutcheon, B., Yarom, Y., Hutcheon, B., and Yarom, Y. (2000). Resonance, oscillation and the intrinsic frequency preferences of neurons. Trends Neurosci. *23*, 216–222. https://doi.org/10.1016/S0166-2236(00)01547-2.
35. Chung, W.G., Jang, J., Cui, G., Lee, S., Jeong, H., Kang, H., Seo, H., Kim, S., Kim, E., Lee, J., et al. (2024). Liquid-metal-based three-dimensional microelectrode arrays integrated with implantable ultrathin retinal prosthesis for vision restoration. Nat. Nanotechnol. *19*, 688–697. https://doi.org/10.1038/s41565-023-01587-w.
36. Kim, E., Jeong, E., Hong, Y.-M., Jeong, I., Kim, J., Kwon, Y.W., Park, Y.-G., Lee, J., Choi, S., Kim, J.-Y., et al. (2025). Magnetically reshapable 3D multi-electrode arrays of liquid metals for electrophysiological analysis of brain organoids. Nat. Commun. *16*, 2011. https://doi.org/10.1038/s41467-024-55752-3.
37. Kong, M., Vong, M.H., Kwak, M., Lim, I., Lee, Y., Lee, S.H., You, I., Awartani, O., Kwon, J., Shin, T.J., et al. (2024). Ambient printing of native oxides for ultrathin transparent flexible circuit boards. Science *385*, 731–737. https://doi.org/10.1126/science.adp3299.
38. Cogan, S.F. (2008). Neural Stimulation and Recording Electrodes. Annu. Rev. Biomed. Eng. *10*, 275–309. https://doi.org/10.1146/annurev.bioeng.10.061807.160518.
39. Güler, A.D., Ecker, J.L., Lall, G.S., Haq, S., Altimus, C.M., Liao, H.-W., Barnard, A.R., Cahill, H., Badea, T.C., Zhao, H., et al. (2008). Melanopsin cells

are the principal conduits for rod–cone input to non-image-forming vision. Nature *453*, 102–105. https://doi.org/10.1038/nature06829.

40. Liu, S., Xiang, K., Lei, Q., Qiu, S., Xiang, M., and Jin, K. (2022). An optimized procedure to record visual evoked potential in mice. Exp. Eye Res. *218*, 109011. https://doi.org/10.1016/j.exer.2022.109011.
41. Rein, B., Ma, K., and Yan, Z. (2020). A Standardized Social Preference Protocol for Measuring Social Deficits in Mouse Models of Autism. Nat. Protoc. *15*, 3464–3477. https://doi.org/10.1038/s41596-020-0382-9.
42. Potrebić, M., Pavković, Ž., Puškaš, N., and Pešić, V. (2022). The Influence of Social Isolation on Social Orientation, Sociability, Social Novelty Preference, and Hippocampal Parvalbumin-Expressing Interneurons in Peripubertal Rats – Understanding the Importance of Meeting Social Needs in Adolescence. Front. Behav. Neurosci. *16*, 872628. https://doi.org/10.3389/fnbeh.2022.872628.
43. Dvoriantchikova, G., Fleishaker, M., and Ivanov, D. (2023). Molecular mechanisms of NMDA excitotoxicity in the retina. Sci. Rep. *13*, 18471. https://doi.org/10.1038/s41598-023-45855-0.
44. Fahrenthold, B.K., Fernandes, K.A., and Libby, R.T. (2018). Assessment of intrinsic and extrinsic signaling pathway in excitotoxic retinal ganglion cell death. Sci. Rep. *8*, 4641. https://doi.org/10.1038/s41598-018-22848-y.
45. Jin, H.-J., Pei, L., Li, Y.-N., Zheng, H., Yang, S., Wan, Y., Mao, L., Xia, Y.-P., He, Q.-W., Li, M., et al. (2017). Alleviative effects of fluoxetine on depressive-like behaviors by epigenetic regulation of BDNF gene transcription in mouse model of post-stroke depression. Sci. Rep. *7*, 14926. https://doi.org/10.1038/s41598-017-13929-5.
46. Tura, A., and Goya-Maldonado, R. (2023). Brain connectivity in major depressive disorder: a precision component of treatment modalities? Transl. Psychiatry *13*, 196. https://doi.org/10.1038/s41398-023-02499-y.
47. Mulders, P.C., van Eijndhoven, P.F., Schene, A.H., Beckmann, C.F., and Tendolkar, I. (2015). Resting-state functional connectivity in major depressive disorder: A review. Neurosci. Biobehav. Rev. *56*, 330–344. https://doi.org/10.1016/j.neubiorev.2015.07.014.
48. Zheng, C., and Zhang, T. (2015). Synaptic plasticity-related neural oscillations on hippocampus–prefrontal cortex pathway in depression. Neuroscience *292*, 170–180. https://doi.org/10.1016/j.neuroscience.2015.01.071.
49. Liu, W., Ge, T., Leng, Y., Pan, Z., Fan, J., Yang, W., and Cui, R. (2017). The Role of Neural Plasticity in Depression: From Hippocampus to Prefrontal Cortex. Neural Plast. *2017*, 6871089. https://doi.org/10.1155/2017/6871089.
50. Le Floch, P., Zhao, S., Liu, R., Molinari, N., Medina, E., Shen, H., Wang, Z., Kim, J., Sheng, H., Partarrieu, S., et al. (2024). 3D spatiotemporally scalable in vivo neural probes based on fluorinated elastomers. Nat. Nanotechnol. *19*, 319–329. https://doi.org/10.1038/s41565-023-01545-6.
51. Jia, L., Sun, Z., Shi, D., Wang, M., Jia, J., He, Y., Xue, F., Ren, Y., Yang, J., and Ma, X. (2019). Effects of different patterns of electric stimulation of the ventromedial prefrontal cortex on hippocampal–prefrontal coherence in a rat model of depression. Behav. Brain Res. *356*, 179–188. https://doi.org/10.1016/j.bbr.2018.08.032.
52. Nobakhsh, B., Shalbaf, A., Rostami, R., Kazemi, R., Rezaei, E., and Shalbaf, R. (2023). An effective brain connectivity technique to predict repetitive transcranial magnetic stimulation outcome for major depressive disorder patients using EEG signals. Phys. Eng. Sci. Med. *46*, 67–81. https://doi.org/10.1007/s13246-022-01198-0.
53. Lee, S.Y., Kozalakis, K., Baftizadeh, F., Campagnola, L., Jarsky, T., Koch, C., and Anastassiou, C.A. (2024). Cell-class-specific electric field entrainment of neural activity. Neuron *112*, 2614–2630.e5. https://doi.org/10.1016/j.neuron.2024.05.009.
54. Li, Y., Kang, C., Qu, X., Zhou, Y., Wang, W., and Hu, Y. (2016). Depression-Related Brain Connectivity Analyzed by EEG Event-Related Phase Synchrony Measure. Front. Hum. Neurosci. *10*, 477. https://doi.org/10.3389/fnhum.2016.00477.
55. Schwartzmann, B., Quilty, L.C., Dhami, P., Uher, R., Allen, T.A., Kloiber, S., Lam, R.W., Frey, B.N., Milev, R., Müller, D.J., et al. (2023). Resting-state EEG delta and alpha power predict response to cognitive behavioral therapy in depression: a Canadian biomarker integration network for depression study. Sci. Rep. *13*, 8418. https://doi.org/10.1038/s41598-023-35179-4.
56. Fingelkurts, A.A., Fingelkurts, A.A., Rytsälä, H., Suominen, K., Isometsä, E., and Kähkönen, S. (2006). Composition of brain oscillations in ongoing EEG during major depression disorder. Neurosci. Res. *56*, 133–144. https://doi.org/10.1016/j.neures.2006.06.006.
57. Olbrich, S., Tränkner, A., Chittka, T., Hegerl, U., and Schönknecht, P. (2014). Functional connectivity in major depression: Increased phase synchronization between frontal cortical EEG-source estimates. Psychiatry Res. Neuroimaging. *222*, 91–99. https://doi.org/10.1016/j.pscychresns.2014.02.010.
58. Fingelkurts, A.A., Fingelkurts, A.A., Rytsälä, H., Suominen, K., Isometsä, E., and Kähkönen, S. (2007). Impaired functional connectivity at EEG alpha and theta frequency bands in major depression. Hum. Brain Mapp. *28*, 247–261. https://doi.org/10.1002/hbm.20275.
59. Hering, H., and Sheng, M. (2001). Dentritic spines : structure, dynamics and regulation. Nat. Rev. Neurosci. *2*, 880–888. https://doi.org/10.1038/35104061.
60. Pchitskaya, E., and Bezprozvanny, I. (2020). Dendritic Spines Shape Analysis—Classification or Clusterization? Perspective. Front. Synaptic Neurosci. *12*, 31. https://doi.org/10.3389/fnsyn.2020.00031.
61. Giovannoni, F., and Quintana, F.J. (2020). The Role of Astrocytes in CNS Inflammation. Trends Immunol. *41*, 805–819. https://doi.org/10.1016/j.it.2020.07.007.
62. Drevets, W.C., Wittenberg, G.M., Bullmore, E.T., and Manji, H.K. (2022). Immune targets for therapeutic development in depression: towards precision medicine. Nat. Rev. Drug Discov. *21*, 224–244. https://doi.org/10.1038/s41573-021-00368-1.
63. Liu, Y., Zhou, L.-J., Wang, J., Li, D., Ren, W.-J., Peng, J., Wei, X., Xu, T., Xin, W.-J., Pang, R.-P., et al. (2017). TNF-α Differentially Regulates Synaptic Plasticity in the Hippocampus and Spinal Cord by Microglia-Dependent Mechanisms after Peripheral Nerve Injury. J. Neurosci. *37*, 871–881. https://doi.org/10.1523/JNEUROSCI.2235-16.2016.
64. Lee, C.H., Ahn, J.H., Chen, B.H., Kim, D.W., Sim, H., Lee, T.-K., Park, J.H., Won, M.-H., and Choi, S.Y. (2021). Differences in TNF-α and TNF-R1 expression in damaged neurons and activated astrocytes of the hippocampal CA1 region between young and adult gerbils following transient forebrain ischemia. Mol. Med. Rep. *24*, 625. https://doi.org/10.3892/mmr.2021.12264.
65. Lu, B., Nagappan, G., Guan, X., Nathan, P.J., and Wren, P. (2013). BDNF-based synaptic repair as a disease-modifying strategy for neurodegenerative diseases. Nat. Rev. Neurosci. *14*, 401–416. https://doi.org/10.1038/nrn3505.
66. Moliner, R., Girych, M., Brunello, C.A., Kovaleva, V., Biojone, C., Enkavi, G., Antenucci, L., Kot, E.F., Goncharuk, S.A., Kaurinkoski, K., et al. (2023). Psychedelics promote plasticity by directly binding to BDNF receptor TrkB. Nat. Neurosci. *26*, 1032–1041. https://doi.org/10.1038/s41593-023-01316-5.
67. Noble, W.S. (2006). What is a support vector machine? Nat. Biotechnol. *24*, 1565–1567. https://doi.org/10.1038/nbt1206-1565.
68. Salcedo-Sanz, S., Rojo-Álvarez, J.L., Martínez-Ramón, M., and Camps-Valls, G. (2014). Support vector machines in engineering: an overview. WIREs Data Min. Knowl. Discov. *4*, 234–267. https://doi.org/10.1002/widm.1125.
69. Farquad, M.A.H., and Bose, I. (2012). Preprocessing unbalanced data using support vector machine. Decis. Support Syst. *53*, 226–233. https://doi.org/10.1016/j.dss.2012.01.016.
70. Belkina, A.C., Ciccolella, C.O., Anno, R., Halpert, R., Spidlen, J., and Snyder-Cappione, J.E. (2019). Automated optimized parameters for

T-distributed stochastic neighbor embedding improve visualization and analysis of large datasets. Nat. Commun. *10*, 5415. https://doi.org/10.1038/s41467-019-13055-y.

71. Morimoto, T. (2025). Transcorneal electrical stimulation: impact on healthcare and future potential. Front. Cell Dev. Biol. *13*, 1569759. https://doi.org/10.3389/fcell.2025.1569759.

72. Yu, W.-S., Kwon, S.-H., Agadagba, S.K., Chan, L.-L.-H., Wong, K.-H., and Lim, L.-W. (2021). Neuroprotective Effects and Therapeutic Potential of Transcorneal Electrical Stimulation for Depression. Cells *10*, 2492. https://doi.org/10.3390/cells10092492.

73. Verma, A., Agadagba, S.K., and Chan, L.L.-H. (2024). Exploring the synergy of the eye-brain connection: neuromodulation approaches for neurodegenerative disorders through transcorneal electrical stimulation. Neural Regen. Res. *19*, 2097–2098. https://doi.org/10.4103/1673-5374.392877.

74. Agadagba, S.K., Eldaly, A.B.M., and Chan, L.L.H. (2022). Transcorneal Electrical Stimulation Induces Long-Lasting Enhancement of Brain Functional and Directional Connectivity in Retinal Degeneration Mice. Front. Cell. Neurosci. *16*, 785199. https://doi.org/10.3389/fncel.2022.785199.

75. Yu, W.S., Aquili, L., Wong, K.H., Lo, A.C.Y., Chan, L.L.H., Chan, Y.-S., and Lim, L.W. (2022). Transcorneal electrical stimulation enhances cognitive functions in aged and 5XFAD mouse models. Ann. N. Y. Acad. Sci. *1515*, 249–265. https://doi.org/10.1111/nyas.14850.

76. Yu, W.S., Tse, A.C.-K., Guan, L., Chiu, J.L.Y., Tan, S.Z.K., Khairuddin, S., Agadagba, S.K., Lo, A.C.Y., Fung, M.-L., Chan, Y.-S., et al. (2022). Antidepressant-like effects of transcorneal electrical stimulation in rat models. Brain Stimul. *15*, 843–856. https://doi.org/10.1016/j.brs.2022.05.018.

77. Pereira, G.C., Piton, E., Bornholdt, J., dos Santos, B.M., de Almeida, A.S., Dalenogare, D.P., Fialho, M.F.P., Becker, G., da Silva Brum, E., Sampaio, T.B., et al. (2023). TRPA1 participation in behavioral impairment induced by chronic corticosterone administration. Psychopharmacology *240*, 157–169. https://doi.org/10.1007/s00213-022-06290-7.

78. Ramón-Moliner, E. (1970). The Golgi-Cox Technique. In Contemporary Research Methods in Neuroanatomy, W.J.H. Nauta and S.O.E. Ebbesson, eds. (Springer), pp. 32–55. https://doi.org/10.1007/978-3-642-85986-1_3.

79. Glaser, E.M., and Van der Loos, H. (1981). Analysis of thick brain sections by obverse—Reverse computer microscopy: Application of a new, high clarity Golgi—Nissl stain. Journal of Neuroscience Methods *4*, 117–125. https://doi.org/10.1016/0165-0270(81)90045-5.